Energy Efficiency First 2 (2025) 100009

Contents lists available at ScienceDirect

Energy Efficiency First

journal homepage: www.journals.elsevier.com/energy-efficiency-first

Operational and economic design of multi-terminal medium DC voltage hybrid renewable energy systems for effective power sharing

M.M. Ahmed [a,d], F.C. Jong [a,c], Lau Wei Kin [a,e], Ahmed M.A. Haidar [a,b,*]

[a] Department of Electrical and Electronic Engineering, Universiti Malaysia Sarawak, Kota Samarahan, Malaysia
[b] School of Engineering, University of Southern Queensland, Toowoomba, Australia
[c] Department of Grid System Operator, Sarawak Energy Berhad, Kuching, Sarawak, Malaysia
[d] Musse Innovative Sdn. Bhd., 93050, Kuching, Sarawak, Malaysia
[e] BOLE MEPF Associates, 98000, Miri, Sarawak, Malaysia

A B S T R A C T

The advancement of multi-terminal medium-voltage direct current (MVDC) technology is accelerating the transition of DC distribution from point-to-point connections to renewable-integrated systems. However, the integration of remote renewable sources introduces challenges in control and economic optimization, particularly for voltage-source converter (VSC)-based designs. Therefore, this paper proposes a multi-terminal MVDC architecture for hybrid renewable energy systems with three primary objectives: to develop an effective power-sharing control using a modular multilevel converter-based topology, to assess the economic feasibility of hybrid configurations under varying load and weather conditions, and to implement real-time monitoring through an Internet of Things-based cloud platform. The scope of this paper encompasses the development and validation of decentralized droop control for reliable power sharing, techno-economic analysis using the hybrid optimization of multiple energy resources (HOMER) for cost and energy optimization, real-time system monitoring through ThingSpeak, and MATLAB-based Internet of Things (IoT) integration. Additionally, it includes transient fault simulations to evaluate voltage stability and system resilience. A generalized framework that combines decentralized droop control and economic optimization is established for system sizing and operational reliability assessment. Simulation results indicate that the proposed system maintains DC voltage deviations within 3 % under steady-state conditions, 3.1 % following AC three-phase faults, and as low as 2.2 % after DC pole-to-pole short-circuit events. The unmet load percentage was extremely low (0.0165 %), while excess energy remained manageable (up to 8 %). The system achieves a levelized cost of energy (LCOE) of 0.4114 $/kWh and a renewable energy share of up to 44 %. These results demonstrate that the proposed MVDC configuration is technically robust, cost-effective, and IoT-enabled, making it well-suited for renewable energy integration in Sarawak, Malaysia.

1. Introduction

Sarawak's renewable energy is recognized as a major asset of the state due to its larger land size compared to other states in Malaysia. This makes the direct current (DC) distribution system a preferable option for large-scale transmission and renewable energy integration, including transportation electrification in Sarawak. The rapid development of multi-terminal voltage source converters in high-voltage DC transmission systems can facilitate the evolution of new topologies for multi-terminal medium voltage DC (MVDC) in distribution systems. The DC system is more economical and efficient in transferring bulk power over long distances with less transmission line control complexity compared to alternating current (AC) [1]. In multi-terminal DC (MTDC) systems, line commutated converters (LCC) and voltage source converters (VSC) are the two most commonly used converter technologies [2]. LCC uses diodes or thyristors as basic switches, and the conversion process of LCC depends on the line voltage of the AC system to which the converter is connected [3]. However, LCC lacks the controllability of DC voltage and can only be used in rectification mode. Generally, the DC in LCC flows in one direction with a constant value. On the AC side, the converter acts as the source of current due to the injection of harmonic currents and grid frequency into the AC network. Therefore, LCC is also known as a current-source converter. Since LCC only allows current to flow in one direction, reverse power flow is achieved by reversing the DC polarity of both substations [4]. With advancements in technology for fully controlled power electronic systems, the VSC employs an insulated gate bipolar transistor (IGBT) for the switching process. This is due to the benefits of additional controllability, as the IGBT can switch on and off many times per cycle. In contrast to LCC, power reversal in VSC is achieved by reversing the direction of current as the VSC maintains a constant polarity of DC voltage, making VSC easy to connect to the MTDC system. There are a few types of VSC commonly used in power

* Corresponding author: Department of Electrical and Electronic Engineering, Universiti Malaysia Sarawak, Kota Samarahan, Malaysia
E-mail addresses: ahahmed@unimas.my, ahmed.haidar@unisq.edu.au (A.M.A. Haidar).

https://doi.org/10.1016/j.eef.2025.100009
Received 11 July 2025; Received in revised form 24 October 2025; Accepted 29 November 2025
Available online 2 December 2025

systems, for instance, two-level, three-level, and modular multilevel converters. In this paper, the modular multilevel converter (MMC) is used in the hybrid design of the MVDC system. This paper goes beyond previous studies by providing a more in-depth analysis of both the techno-economic viability and cloud-based monitoring aspects.

1.1. Review of multi-terminal DC systems

It is noticeable that the integration of renewable energy sources (RES) into the power grid is getting more attention in recent studies. This makes the planning and design of the hybrid AC/DC distribution network crucial in the integration stage to ensure a stable supply to DC infrastructures and transportation facilities [5]. Consequently, different MTDC systems are reviewed in this section, such as topologies, types of converters, and voltage control schemes to develop a customized configuration of voltage source converter-based multi-terminal direct current (VSC-MTDC), considering techno-economic feasibility [6] and system monitoring.

Researchers have focused on refining the topologies of power grid transmission and distribution systems to enhance overall performance. Fig. 1 depicts the topological classification of hybrid AC/DC distribution systems [7]. As multi-terminal DC grid technology arises, the types of topologies have been revised with different configurations to suit the proposed MTDC system. A few communication topologies for multi-terminal high-voltage DC systems have been examined [8]. The point-to-point topology's limited flexibility and susceptibility to disruptions make it unsuitable for many applications. The loss of connection between two points could occur during line fault conditions. Hence, it is not operationally flexible. The ring topology, which is connected within a loop, is a simple construction and more flexible, as it can operate under closed and open loop conditions with a degree of stability. However, it requires a fast communication network and moderate reliability. Additionally, the long-distance transmission lines result in greater losses [9]. While ring topology offers strong stability, the voltage control can be challenging. Adjusting the voltage at one point in the ring can affect the voltage at other connected buses, potentially impacting the entire system. The radial topology consists of a central bus to control the power flow of other branches. Although this topology is simple and easy to construct, the entire system would fail if the central bus stopped operating. Another type of MTDC system, known as meshed topology, has better stability and power capability than other topologies. The reason for this is that all voltage source converters are connected. However, the cost of this topology is higher as the control connection covers the whole system [10]. The MTDC systems are used for high voltage direct current (HVDC) long transmission lines and the AC-DC converters, and these systems usually employ LCC for power conversion. The common fault in these systems is communication failure, and to overcome this issue, the thyristor-based full-bridge module (TFBM) is integrated into LCC to provide additional commutation voltage support to the LCC-HVDC system [11,12]. A four-pole system is introduced in Ref. [13], which consists of two positive and two negative poles. The proposed configuration converts the conventional two-pole system with double 12-pulse converters into a four-pole system with quad 12-pulse converters. In Ref. [14], fixed parallel capacitors have been added at the valve side of the LCC-HVDC transformer converter to reduce its size, because AC filters are no longer needed. On the same note, to increase active power transfer, the authors in Ref. [15] proposed adding a series compensated capacitor at the AC side transformer. On one hand, the modifications made in Refs. [13,14], and [15] improved the system's reliability. On the other hand, the addition of components caused a slight increase in power loss. LCC technology is more suitable for an HVDC transmission system than the MVDC system. VSC technology utilizes IGBT to enable independent on/off switching of current, regardless of the AC voltage. In such a regime, the VSC operates at high-frequency pulse width modulation (PWM) to control its phase angle and amplitude while maintaining a constant voltage and reducing harmonic distortion. It has the independent capability to control active and reactive power with a high degree of flexibility [16]. The first configuration of VSC started with a two-level converter that consisted of six-pulse bridge IGBTs and a DC capacitor. However, employing the PWM technique in this configuration resulted in high switching losses, making the efficiency of the conventional two-level converter very poor. The two-level converter has been enhanced by incorporating two distributed cell capacitors per three-phase. This modification simplifies power circuit control and improves transient response [17], but the system cost increases due to the need for expensive filters. In Ref. [18], blocking capacitors and switches have been replaced in the conventional three-level converter with cascaded sub-modules. This can provide higher efficiency and lower switching loss, as compared to the two-level converter [18,19]. VSC has several advantages over LCC, including

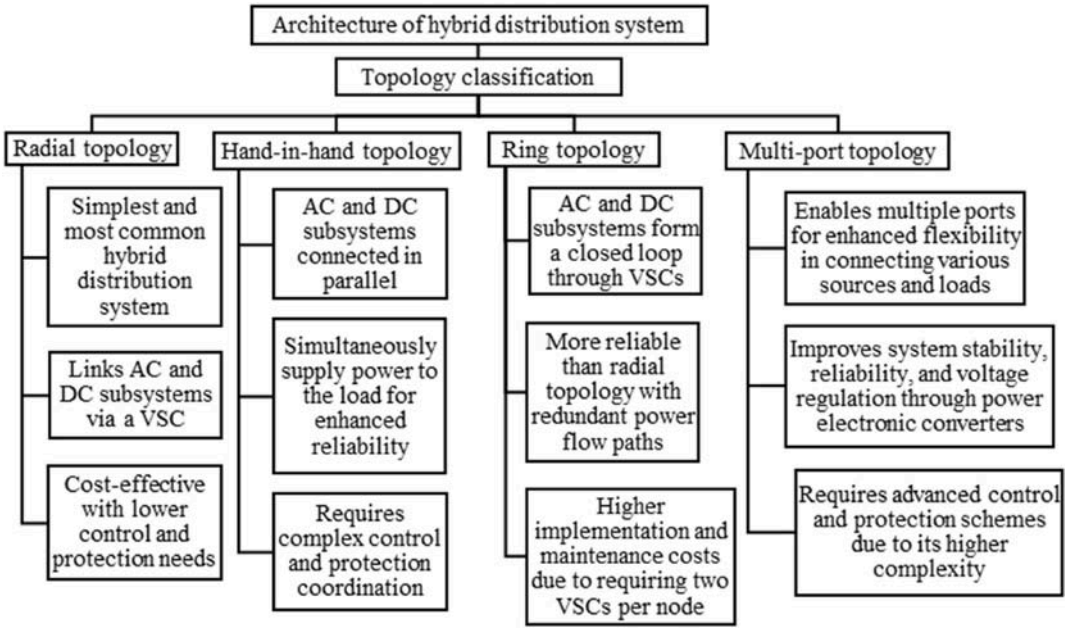

Fig. 1. Topological classification of hybrid AC/DC distribution systems.

better control over power flow, improved fault tolerance, and reduced harmonic distortion. The VSC technology has indeed seen significant advancements in recent years, resulting in higher efficiency, improved reliability, and better performance. As a result, VSC-based HVDC systems are gaining popularity in many applications, such as renewable energy integration, offshore wind farms, and interconnecting grids.

Recently, MMC-based VSC technology has received more attention in the design of MTDC systems due to its lower harmonic distortion, lower power losses, and higher scalability [20]. It comprises upper and lower arms with a series connection of half-bridge (HB) or full-bridge (FB) modules. The HB configuration employs two IGBTs per submodule, while the FB configuration uses four. HB-MMC offers advantages like voltage scaling, harmonic elimination, and reduced fault current and power losses due to its multilevel switching. However, it cannot block DC fault currents from the AC system. Therefore, FB-MMC is introduced to override the overcurrent [21]. It is worth mentioning that the VSC technology, initially developed for HVDC systems, has been adopted for use in multi-terminal DC (MTDC) systems. The modular embedded multilevel converter offers a significant advantage by reducing both energy storage requirements and power losses in semiconductor devices. Specifically, utilizing thyristors can decrease the system's energy storage needs by approximately 50 % [22]. Thus, the system complexity, weight, volume, loss, and cost are significantly reduced, while retaining similar performance. The MMC is capable of exchanging power among distributed sources and loads in the connected microgrid owing to its modular feature [23]. With this advantage, the optimal operation of a hybrid AC/DC system for medium and low voltage levels can be achieved using the MMC-based VSC. The master-slave control method is a well-established approach in multi-terminal VSC HVDC systems, as it maintains a fast dynamic response with minimal interference between voltage regulators. This type of control scheme is simple in terms of implementation and control design; however, it requires high-speed and accurate communication between DC terminals to coordinate the voltage control. Generally, in the MTDC grid, the master terminal must have a large power rating, and the connected AC system must be sufficient to accommodate all the power imbalances of the slave terminals [24–26]. The voltage margin method is a modification of the master-slave control method, and its operational principle is that, when the system operates within a normal operating voltage margin, the terminals operate in constant power mode. However, when the voltage deviates from the set margin, the terminal switches to constant DC voltage mode to prevent further deviation by fixing the voltage within the margin limit. Although the voltage margin method is known for its reliability due to the fixed DC voltage working point, which allows for precise power flow control, its dynamic response is slow since the control system needs time to adjust the voltage to compensate for changes in the grid or load. It is also difficult to configure the voltage margins to satisfy both steady-state and dynamic conditions in a larger-scale network [24,26]. A simple configuration of DC voltage droop control has then been proposed to overcome the drawbacks of the previously mentioned methods. It can manage DC voltage regulation between multiple converter terminals in the DC system to share the unbalanced active power during the dynamic state. Further, if one of the DC regulating terminals fails, the remaining terminals can still share the voltage control accountability. The main drawback of this method lies in the DC voltage working point, which is not fixed and hence, it is difficult to control the power flow precisely [24–26].

Recent studies in the field of hybrid systems have focused on developing innovative features and voltage regulation strategies for microgrids and grid-connected renewable energy systems to facilitate smooth coordination [27]. Considering the above discussions on the DC system control, an energy management strategy based on a novel dimension for the PI controller design has been proposed to stabilize the DC bus voltage [28]. The primary objective is to maintain a 400V DC bus voltage despite fluctuating loads by using buck-boost converters to manage power flow from supercapacitors and batteries. The control strategy in this approach ensures a robust solution for voltage regulation during variable power demands. Ref [29] investigated the implementation of low-voltage DC systems that supply current to the lighting system using cloud platform control and management. In such an approach, additional attention is required to enable proper energy management and ensure the stability of intelligent management and control. Generally, the operation of the smart grid requires advanced and intelligent algorithms with sensor-based protection, such as the phasor measurement unit, which provides faster and more accurate real-time data acquisition [30–32]. Nowadays, energy management of grid-integrated renewable resources is more popular with the use of smart energy meters installed at distribution transformer locations [33, 34]. The meters contain electronic sensors and intelligent devices for data collection that can be stored in the cloud and then monitored in real-time through the Internet [35]. The key principle of cloud computing can be understood as the distribution of services across multiple computers to achieve virtualization of the intended system, as it is the most efficient technique for resource optimization and cost reduction [36]. The cloud-based framework was proposed in Ref. [37] to provide customer-oriented energy management for green communities that have been formed as virtual retail energy providers.

While there is extensive research on HVDC systems, including multi-terminal configurations, the literature indicates a gap in the detailed techno-economic analysis specifically focusing on the feasibility of multi-terminal MVDC systems. Additionally, performance prediction through condition monitoring was overlooked in the previously proposed designs of MTDC systems. Hence, this paper evaluates the optimal design of such systems by analyzing different configurations in terms of electricity price, operating cost, and net present cost, considering emission reduction. Furthermore, the paper introduces a platform for condition monitoring evolved specially to suit the operation of the MTDC system in a cloud environment. The following subsection highlights in detail the main contribution of this paper. It is to be noted that the development of a new voltage control method for the MTDC system is out of the scope of this paper.

1.2. Contribution and originality

Many studies and practical implementations of MTDC systems have focused on high-voltage applications. For instance, the Zhoushan ±200 kV, five-terminal MTDC system presented in Ref. [38] is a prominent example of high-voltage DC systems used in related works. The Nanao station was developed with three terminals and a parallel point-to-point topology at the DC voltage level of ±160 kV [39]. Ref [40] developed a four-terminal radial topology high voltage DC system at ±320kv DC, while [41] researched the optimal operation of a ±400 kV MTDC system in a ring topology. As technology advances, more research has started to focus on MTDC systems with Medium and Low voltage levels. However, a few MV-MTDC systems have been proposed with five terminals with ring topology at DC voltage levels of ±5 kV to ±15 kV [42–44]. The four-terminal MVDC system developed at the ±15 kV level in ring topology can operate with good availability and reliability [44]. From the aspects discussed above and the comparison demonstrated in Table 1, this paper proposes a four-terminal ring topology and modular multilevel converter-based VSC configuration for a 15 kV DC voltage. The ring topology was chosen as a pilot study for Sarawak, Malaysia, due to its flexibility and high stability. While VSC-MTDC systems may experience increased power losses and more complex voltage control for long transmission lines, they offer advantages for medium and short distances due to their superior reactive power control capabilities compared to LCC. In particular, to comply with the national grid code and standards, the MMC-based VSC-MTDC system has been selected for study with a four-terminal ring topology. This is a crucial step to meet the requirement for connecting the RES with medium and low voltage levels in Sarawak. As such, the main contributions of this paper are as follows:

Table 1
Comparison between the existing MTDC system and the proposed scheme.

References (including this paper)	Types of hybrid generation	Voltage level	Number of terminals	Topology	Types of converters	Condition monitoring	Techno-economic analysis
[38]	DC grid and wind farms	±200 kV DC	Five	Radial	MMC	No	No
[39]	AC grid and wind farms	±160 kV DC	Three	Point-to-point	MMC	No	No
[40]	AC grid	±320 kV DC	Four	Radial	VSC	No	No
[41]	Wind farms	±400 kV DC	Three	Ring	VSC	No	No
[42]	AC grid and solar photovoltaic (PV)	10 kV DC	Five	Ring	3-Level VSC	No	No
[43]	AC grid	±5 kV DC	Five	Ring	2-Level VSC	No	No
[44]	AC grid	±15 kV DC	Four	Ring	VSC	No	No
[45]	AC grid, wind turbine, solar PV and energy storage	Not stated	Two	Radial	Generic	No	No
[46]	AC grid and wind farms	±500 kV DC	Two	Radial	MMC	No	No
[47]	AC grid and wind farms	±500 kV DC	Five	Ring	VSC	No	No
The proposed design in this paper	AC grid, hydropower, wind farms, solar PV and energy storage.	15 kV DC	Four	Ring	MMC	Yes	Yes

- Modelling the DC power infrastructures for multi-terminal medium voltage as sustainable sources of hybrid renewable energy for distribution and transportation networks, by incorporating the control algorithm of the MMC-based VSC-MTDC embedded in Simscape Electrical in the MATLAB environment.
- Dynamic operation assessment under varied circumstances to validate the robustness of the proposed design behavior and response of the control algorithm.
- Extensive techno-economic analysis for estimating the better dynamic value of energy cost based on the worst condition of renewable generation uncertainties.
- Integrating the cloud-based monitoring platform with the MTDC system to evaluate the condition of system parameters in real-time using the Internet of Things (IoT).

The novelty of this work is the development of a four-terminal 15 kV MVDC hybrid renewable architecture that integrates multiple energy sources, including the AC grid, hydropower, wind, solar PV, and energy storage, within a unified framework. In contrast to previous studies summarized in Table 1, which focused on single-source or limited hybrid configurations without detailed analysis, the proposed system adopts a ring-type MMC-based topology combined with real-time IoT-based condition monitoring and HOMER-assisted techno-economic optimization. This integrated approach enables continuous monitoring of system performance, evaluation of cost and energy efficiency, and improvement of operational reliability under different load and fault conditions. The comprehensive integration of multi-source coordination, digital monitoring, and economic optimization presented in this work addresses a significant gap in the existing research on MVDC hybrid energy systems.

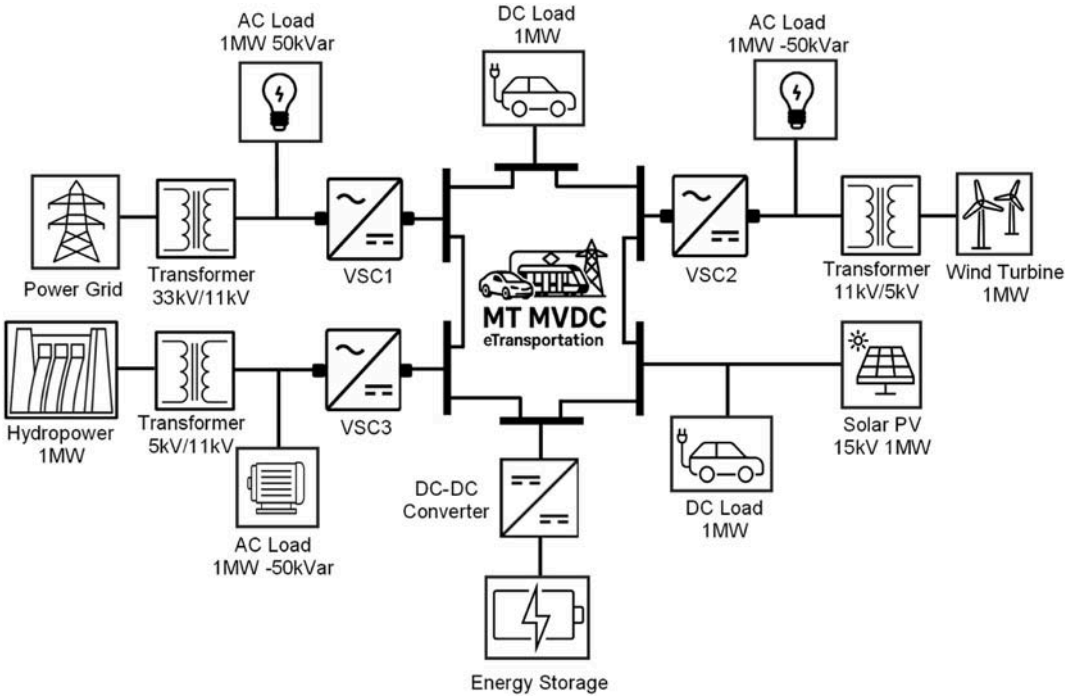

Fig. 2. The proposed design of the multi-terminal MVDC system of 15 kV DC.

2. Customized multi-terminal MVDC design

The integration of renewable energy sources into DC transportation and charging stations is crucial for creating a sustainable and efficient smart city ecosystem. Therefore, a customized power system design with integration of RES is necessary to feed different load types while minimizing environmental impact. Fig. 2 demonstrates the proposed multi-terminal medium voltage design of the hybrid renewable energy-based distribution and transportation networks, where multiple VSCs are interconnected via a medium voltage MVDC. The Simulink model of the four-terminal DC system with associated sources has been developed and tested under various operating conditions. The described design features of three AC terminals and one DC terminal interconnected in a ring topology, operating at a voltage of 15 kV. The four terminals represent the AC power grid and renewable power stations such as hydro, wind, and solar PV. While each renewable generation at different locations supplies its distribution system, it also steps up the voltage to 15 kV DC to be connected in a ring topology for power-sharing purposes.

2.1. Modelling the topology of the proposed MT MVDC system

The current studies primarily focus on traditional modelling approaches for designing multi-terminal MVDC systems, lacking technical-economic analysis, validation of transient behaviors, and determination of the precise dynamic energy price for optimal configuration. Hence, such a modelling method does not ensure the stability and economic durability of the MT MVDC system in terms of energy cost and energy management. Referring to Fig. 2, the general power balance of the system, which includes the integration of RES and energy storage (ES), is represented by (1) [48]. Where $P_G(t)$, $P_L(t)$, and $P_{loss}(t)$ are conventional power generation, electrical load, and power loss respectively; $P_{RES}(t)$ is the power injection from RES as given in (2); $P_{wind}(t)$, $P_{PV}(t)$, and $P_{hydro}(t)$ are the power generation from wind turbines, solar PV and hydro respectively; $P_{ES}(t)$ is the power of storage system. Neglecting reactive power and the phase angle in the load flow analysis, the simplified power flow equation in (2) can be applied to the multi-terminal MVDC system. Where $Y_{DC,ij}$ is the admittance between any DC buses (i and j) with voltage $V_{DC,i}$ and $V_{DC,j}$; n is the number of buses.

$$P_G(t) + P_{RES}(t) + P_{ES}(t) = P_L(t) + P_{loss}(t) \quad (1, a)$$

$$P_{RES}(t) = P_{wind}(t) + P_{PV}(t) + P_{hydro}(t) \quad (1, b)$$

$$P_{DC,i} = \sum_{j=1}^{n} \left|V_{DC,i}\right|\left|V_{DC,j}\right|\left|Y_{DC,ij}\right|;\ j \neq i \quad (2)$$

The PV array power output in (2) at time t is calculated using (3), which considers the temperature de-rating factor. Y_{PV} signifies the PV-rated power in kW, whereas f_{PV} is the de-rating factor that accounts for PV system efficiency. G denotes the solar insolation in practical conditions (kW/m^2) while the G_{stc} is at standard testing conditions. α_{PV} is the temperature coefficient of the PV module (%/°C); T_c signifies the PV cell temperature at the practical conditions, where $T_{c,stc}$ is at standard test conditions.

$$P_{PV} = Y_{PV} f_{PV} \left(\frac{G}{G_{stc}}\right)\left(1 + \alpha_{PV}\left(T_c - T_{c,stc}\right)\right) \quad (3)$$

The optimal capacity of the hydro-generator at a specific time, considering water flow rate, water level, turbine efficiency, and water density, can be determined using (4). Where η_h , g, and ρ_{wat} are the hydro turbine efficiency, gravitational acceleration, and water density, respectively. Q_t denotes the flow rate through the turbine, whereas h_{net} is the net head; h denotes the existing head, and f_h is the pipe head losses.

$$P_{hydro}(t) = \eta_h \times g \times h_{net} \times \rho_{wat}(t) \times Q_t(t) \quad ;\{h_{net} = h(1 - f_h) \quad (4)$$

The power grid generation that acts as a backup source for the multi-terminal MVDC system is determined using (5), which is modeled based on the fuel consumption pattern in (6) as a function of electrical output. P_{rat} is the rated generator power output, η_g denotes power grid generation efficiency; A_g and B_g are fuel consumption coefficients. When the MT MVDC system draws power from the grid, additional carbon dioxide (CO2) emissions are released due to the grid's reliance on various power sources. The total emissions "E" represent the actual CO2 released (kg) for the total power consumed, calculated using the grid emission factor, EF (kg CO2 per kWh), and the overall emission reduction efficiency, ER (%) of the system.

$$P_G(t) = P_{rat}(t) \times \eta_g \quad (5)$$

$$F_g = A_g P_{ds}(t) + B_g P_{rat}(t) \quad (6)$$

$$E = P_G^{total} \times EF \times (1 - ER/100) \quad (7)$$

The power in the wind is calculated using (8), where p is the air density, A is the wind cross-sectional area, and v wind velocity. N_g , N_t, and W_p are the wind generator efficiency, wind turbine efficiency, and power coefficient of the wind turbine, respectively. To represent the variability of the load profile "P_{lp}", a random value is assumed in a bounded range of "ΔP_{lp}" as given in (9).

$$P_{wind}(t) = \frac{1}{2} p A v^3 N_g N_t W_p \quad (8)$$

$$P_{varlp}(t) = P_{lp} \mp \Delta P_{lp} \quad (9)$$

The charge (+) or discharge (−) power of the battery pack is indicated by the state of charge (SOC). In this sense, the flow of power into or from the energy storage system at any given time "t" is expressed in (10) [48]. η_{co} denotes the efficiency of the charging converter; $P_{ES}(SOC^0)$ is the power at the initial SOC; DOD signifies the depth of discharge; P_{ES}^{min} and P_{ES}^{max} are the minimum and maximum power limits. The inverter is the main element of the VSC, and its capacity can be computed by (11), where P_{AC}^{max}, η_{inv} and σ_{sf} are the maximum AC load, inverter efficiency, and safety factor, respectively.

$$P_{ES}(SOC) = P_{ES}(SOC^0) \pm \eta_{co} \sum_{k=0}^{t} P_{ES}(k) \begin{cases} P_{ES}^{min} \le SOC \le P_{ES}^{max} \\ P_{ES}^{min} = (1 - DOD) P_{ES}^{max} \end{cases} \quad (10)$$

$$P_{inv} = \left(\frac{P_{AC}^{max}}{\eta_{inv}}\right)\sigma_{sf} \quad (11)$$

2.2. Modelling the multi-level converter-based VSC

The proposed multi-level converter-based VSC (MMC-VSC) utilizes a modular structure with six half-bridge submodules (HBSMs), divided into three upper and three lower arms. Each submodule contains two IGBTs. Fig. 3 (a) illustrates one of the HBSMs and its output waveform, whereas the configuration of a single MMC-VSC is shown in Fig. 3 (b). The configuration of the Cockcroft-Walton voltage multiplier (CWVM)-based DC-DC converter is depicted in Fig. 3 (c). Referring to Fig. 3, the DC capacitor voltage in (12) is regulated by controlling the IGBTs S1 and S2. The DC capacitor's current depends on the state of S1 and S2 and can be calculated using (13). The switching state of HBSM and its voltage output are illustrated in Table 2. When the switch is on, the AC output voltage is indeed equal to v_c. In this mode, v_c increases in the positive direction of the current and decreases in the negative direction of the current. The AC output voltage of a half-bridge submodule is indeed dependent on the state of its switches and the voltage across the DC capacitor. When the switch is off, the AC output voltage is zero, and v_c remains constant. The AC output voltage of the half-bridge submodule can be represented in terms of the DC capacitor voltage and the switching state of S1 as indicated by (14).

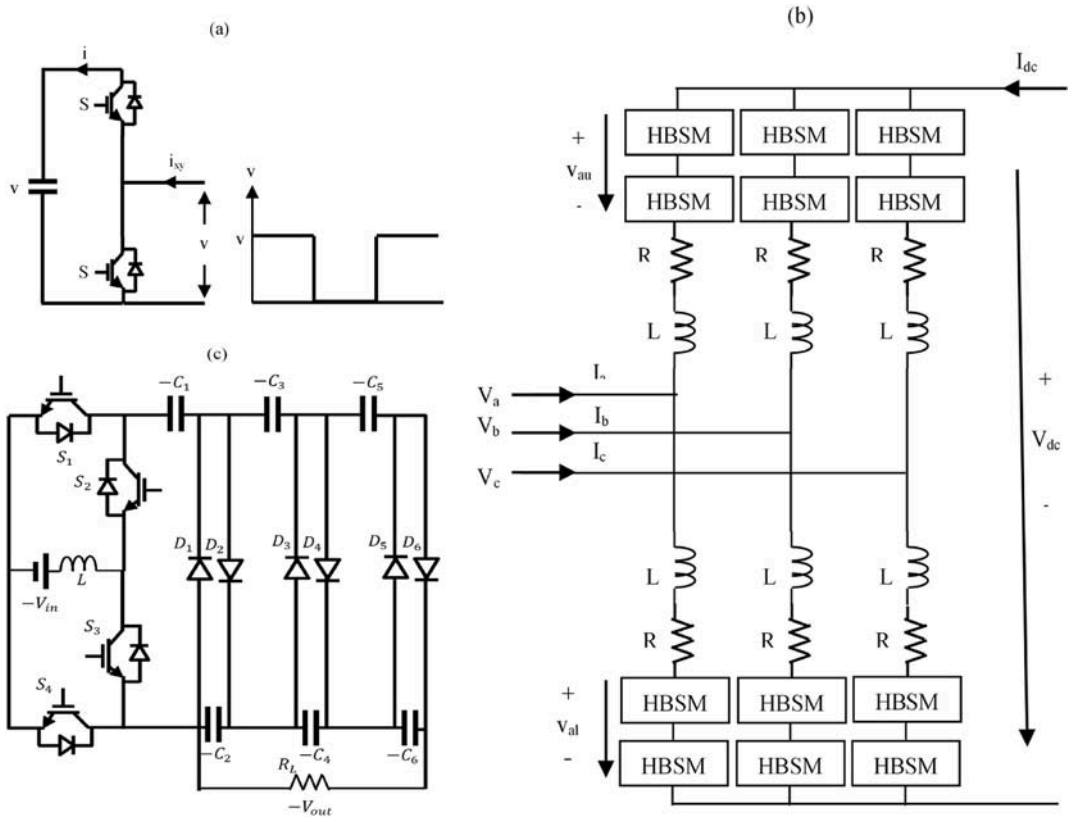

Fig. 3. (a) MMC-based VSC: HBSM and its output waveform; (b) configuration of single MMC-VSC; (c) configuration of CWVM-based DC-DC converter.

Table:2
Switching states of HBSM and output voltage.

State	S_1	V_F	$i_{xy}>0$	$i_{xy}<0$
1	1	v_c	v_c increase	v_c decrease
2	0	0	–	–

$$v_c = \frac{1}{C}\int_{0+}^{t} i_c\, dt \tag{12}$$

$$i_c = S_1 i_{xy} \tag{13}$$

$$v_{ac} = S_1 v_c \tag{14}$$

The upper and lower arm voltages of MMC-VSC can be calculated by applying (15–18) "Kirchhoff's voltage law". Here, u_{au} and u_{al} are upper and lower arm voltage respectively; i_{au} and i_{al} are upper and lower arm current respectively; V_{ao} is AC voltage; V_{dc} is DC voltage; S_{au} is the conduction state of upper arm IGBTs; S_{al} is conduction state of lower arm IGBTs; V_{cau} is voltage across capacitor at upper arm; V_{cal} is voltage across capacitor at lower arm; L is inductance; R is resistance.

$$V_{ao} = \frac{1}{2}V_{dc} - V_{au} - L\frac{di_{au}}{dt} - R_{iau} \tag{15}$$

$$V_{ao} = -\frac{1}{2}V_{dc} + V_{al} + L\frac{di_{al}}{dt} + R_{ial} \tag{16}$$

$$V_{au} = \sum_{k=1}^{n} S_{auk}\cdot V_{cauk} \tag{17}$$

$$V_{al} = \sum_{k=1}^{n} S_{alk}\cdot V_{calk} \tag{18}$$

The upper and lower arm currents can be calculated by applying Kirchhoff's current law using (19) and (20). Where, i_{au} and i_{al} are upper and lower arm currents, respectively. i_a is the AC of phase A; i_{dc} is the DC; i_{diff} is the circulating current of the AC component; V_{dc} is then calculated by combining (17) and (18) to obtain (21).

$$i_{au} = -\frac{1}{2}i_a + \frac{1}{3}i_{dc} + i_{diff} \tag{19}$$

$$i_{al} = \frac{1}{2}i_a + \frac{1}{3}i_{dc} + i_{diff} \tag{20}$$

$$V_{dc} = V_{au} + V_{al} + L\frac{di_{au}}{dt} + L\frac{di_{al}}{dt} + R_{i_{au}} + R_{ial} \tag{21}$$

Referring to Fig. 3 (c), the energy storage is connected to a CWVM-based transformerless high-step DC-DC converter, which consists of four IGBTs, six capacitors, and six diodes. Due to its high voltage gain behavior, it is suitable for low-level DC generation such as PV and batteries [49]. The capacitor voltage is represented by (22), where V_{cn} is the n-th capacitor voltage and V_{in} is the amplitude of the input voltage. The output voltage "V_{out}" is calculated by summing the voltages across even-numbered capacitors using (23). Referring to Fig. 1, in the Simulink model, the DC-DC converter is used to step up the voltage from an energy storage system to 15 kV DC, following the approach described in Ref. [50].

$$V_{cn} = \begin{cases} V_{in}\ for\ n = 1 \\ 2V_{in}\ for\ n = 2, 3, \ldots, N \end{cases} \tag{22}$$

$$V_{out} = \sum_{n=2,4,\ldots}^{N} V_{cn} = N\cdot V_{in} \tag{23}$$

2.3. Control scheme of the MT MVDC system

The multi-terminal MVDC system is controlled by using the generalized voltage droop control strategy in a decentralized manner, as illustrated in Fig. 4. The configuration in this figure shows the single-line diagram of the AC grid terminal with the generalized droop control scheme. The three-phase voltage and current of the VSC are measured and transformed into the d-q rotating reference frame through the Park Transformation. Since the VSC is connected to the grid, the phase angle "ωt" is obtained from the phase-locked loop (PLL). Referring to Fig. 4, the reference current signals obtained from the proportional and integral (PI) of the outer controllers serve as inputs to the inner controller for AC and DC regulation, including the active and reactive power control. Hence, the inner controller generates a voltage reference signal, which is then fed into the PWM gate signal generator to control the switching of the MMC's power semiconductor devices [51]. The outer controller input error of the DC voltage-active power droop control is calculated by (24), where V_{dc}^{mea} is the measured DC voltage of the VSC, K_v denotes the voltage gain error, and $V_{dc,ref}^{P_{reg}}$ is the reference DC voltage from the active power regulator and can be obtained by (25). Where P_{con}, P_{ref}, and K_P are the VSC output active power, reference active power, and the active power gain error, respectively. The input error is regulated to zero by the PI controller. Therefore, P_{con} during steady-state operation satisfies (26).

$$e = \left(V_{dc}^{mea} - V_{dc,ref}^{P_{reg}}\right)K_v \tag{24}$$

$$V_{dc,ref}^{P_{reg}} = \left(P_{con} - P_{ref}\right)K_P \tag{25}$$

$$P_{con} = P_{ref} + \left(\frac{V_{dc}^{mea}}{K_P}\right) \tag{26}$$

The output active power of VSC in (25) and (26) is related to its measured DC voltage in (24), hence, when the power exceeds in the MTDC system and results in an increase of overall DC grid voltage, the DC voltages of all VSCs with droop control follow the generalized droop characteristics to increase output power to suppress voltage rise. In this case, more than one VSC can be involved in this process without affecting the regulation of DC grid voltage, as each VSC maintains its local terminal in a decentralized manner. The voltage droop control demonstrates high reliability in coordination control among VSCs. However, the active power of VSC is vulnerable to DC voltage disturbance. The reason for this is the influence of power fluctuation from the RER and transmission line impedance.

As the DC voltages at different VSC terminals differ according to the directions of power flows and power balance in the MTDC network [52], the transient behaviors of the optimized configuration have been analyzed by applying faults at the DC side. This is a crucial step to ensure the resilience of control systems to withstand the worst-case disturbances, such as pole-to-pole DC short-circuit fault. Such a type of short-circuit fault is a severe condition in AC/DC hybrid distribution networks and can produce a high fault current that may damage the equipment. Fig. 5 (a) illustrates the diagram of the pole-to-pole DC short-circuit fault and the response of the control scheme presented in this section. As seen in this figure, the converter's outlet consists of two parallel capacitors, C_P and C_N, used to stabilize the DC side voltage. Let's consider that at t = 1.5 s, a fault has occurred at the DC side of the power grid. When the fault occurs, the capacitors C form an RC oscillating circuit with the DC distribution lines R_d because the DC side voltage is higher than the AC side. At this time, the parallel capacitors discharge and supply current to the fault. The current flow during the fault condition is shown in Fig. 5 (b). When both capacitors are fully discharged, the voltage of each capacitor drops to zero. At this stage, all HBSMs are switched on, hence no current is flowing to the capacitors. Here, the AC side is equivalent to a three-phase short-circuit fault, as shown in Fig. 6 (a). After that, the switching of HBSM-based modular VSC is managed by the control scheme depicted in Fig. 4. In such a condition, the current is fed from the AC side to the fault, as depicted in Fig. 6 (b).

3. Techno-economic assessment of the proposed design

Economic analysis is crucial when designing a multi-terminal MVDC system. In this sense, the proposed design in Fig. 2 has been modeled

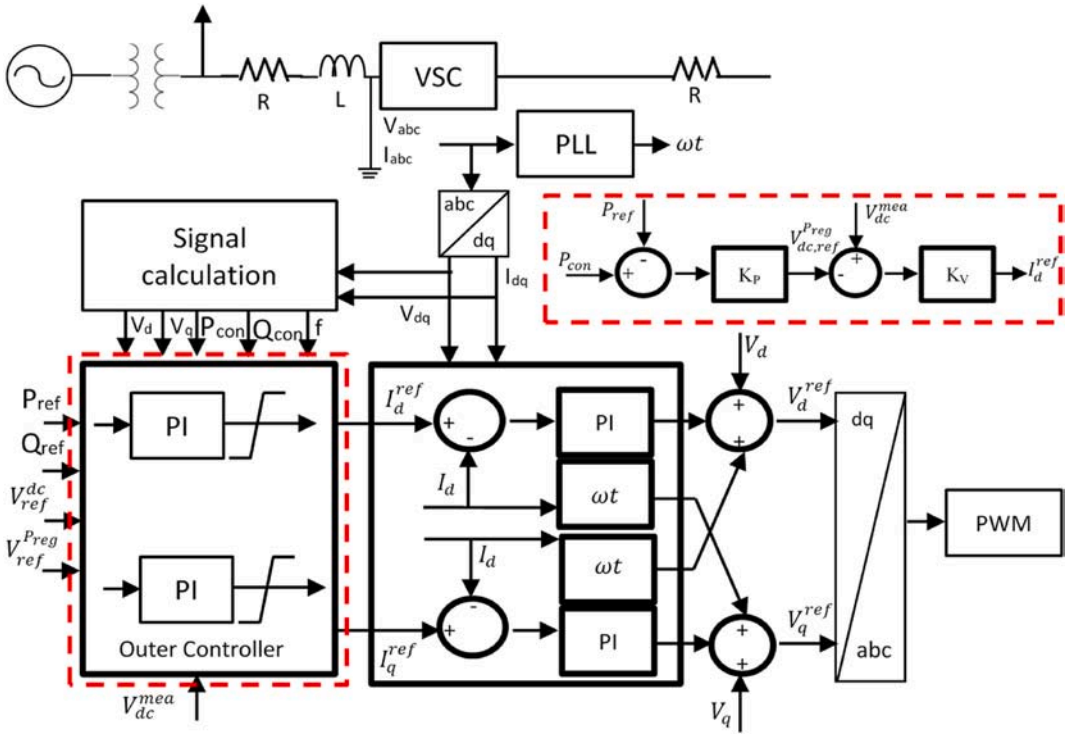

Fig. 4. Generalized droop control scheme.

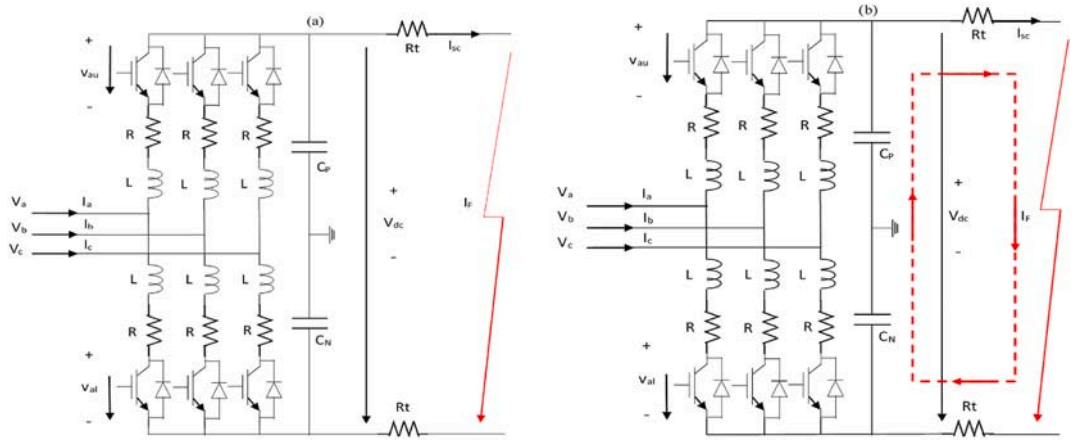

Fig. 5. Pole-to-pole: (a) DC short-circuit fault; (b) parallel capacitors discharge.

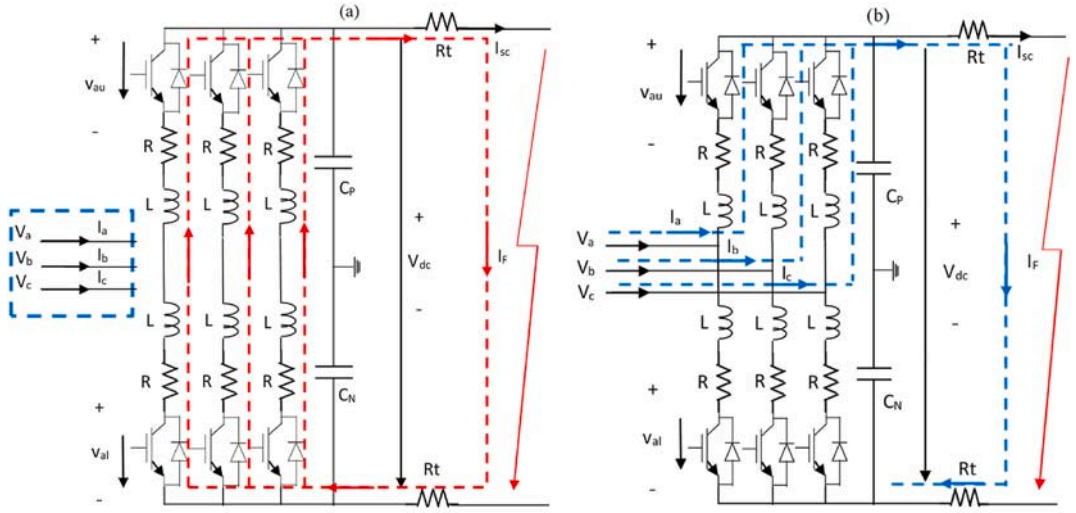

Fig. 6. Pole-to-pole: (a) all HBSMs switched on; (b) AC feeds the fault.

with various types of energy resources in grid-integrated and islanded modes to evaluate the optimal configurations based on technical feasibility and economic viability. The hybrid optimization of multiple energy resources (HOMER) [53] was selected to analyze the economic and environmental viability. In the economic optimization, as specified by (27) and simplified in Fig. 7, the load-following dispatch strategy was applied to manage power generation in response to fluctuating load demands in time steps, incorporating climate and monetary data needed to optimize energy production and cost. In this method, the proprietary derivative-free algorithm in HOMER was used to search for a configuration with the lowest net present cost (NPC). As the mathematical modeling of techno-economic analysis is well documented in Refs. [54–56], details are not presented in this paper. The actual market price of each component has been used to calculate the NPC, cost of energy (COE), and the operating cost for each configuration using (28), (29), and (30), respectively. Where t denotes the period (years); C_t is the revenues for t period; r signifies the rate of discount; C_0 is the cost of initial investment; $C_{ann.tot}$ represents the total annualized cost of all components; E_{ue} means the total amount of useful energy produced by the system per year; $C_{ann.cap}$ denotes total capital cost.

$$min\left(\sum system\ cost - project\ revenue\right) \tag{27}$$

$$NPC = \sum_{t=1}^{t=N} \frac{C_t}{(1+r)^t} - C_0 \tag{28}$$

$$COE = \frac{C_{ann.tot}}{E_{ue}} \tag{29}$$

$$C_{oper} = C_{ann.tot} - C_{ann.cap} \tag{30}$$

The value remaining in the system component at the end of the project lifetime is calculated using (31). The system's total cost in (32) is the annualized value of the total net present cost. R_{rem} is the remaining life while R_{comp} is the component lifetime; C_{rep} represents the component replacement cost; NPC_{tot} is the total NPC, i denotes the discount rate in a year, R_{proj} is the project lifetime, whereas CRF is the function of capital recovery factor. The robustness of the economic models to variations of AC or DC loads and renewable generation in the MVDC system is measured through the sensitivity index (SI) using (33). It is defined as the ratio of change in the responding variables to the change in the manipulated variables.

$$SV = C_{rep}\frac{R_{rem}}{R_{comp}} \tag{31}$$

$$C_{ann.tot} = CRF\left(i, R_{proj}\right).NPC_{tot} \tag{32}$$

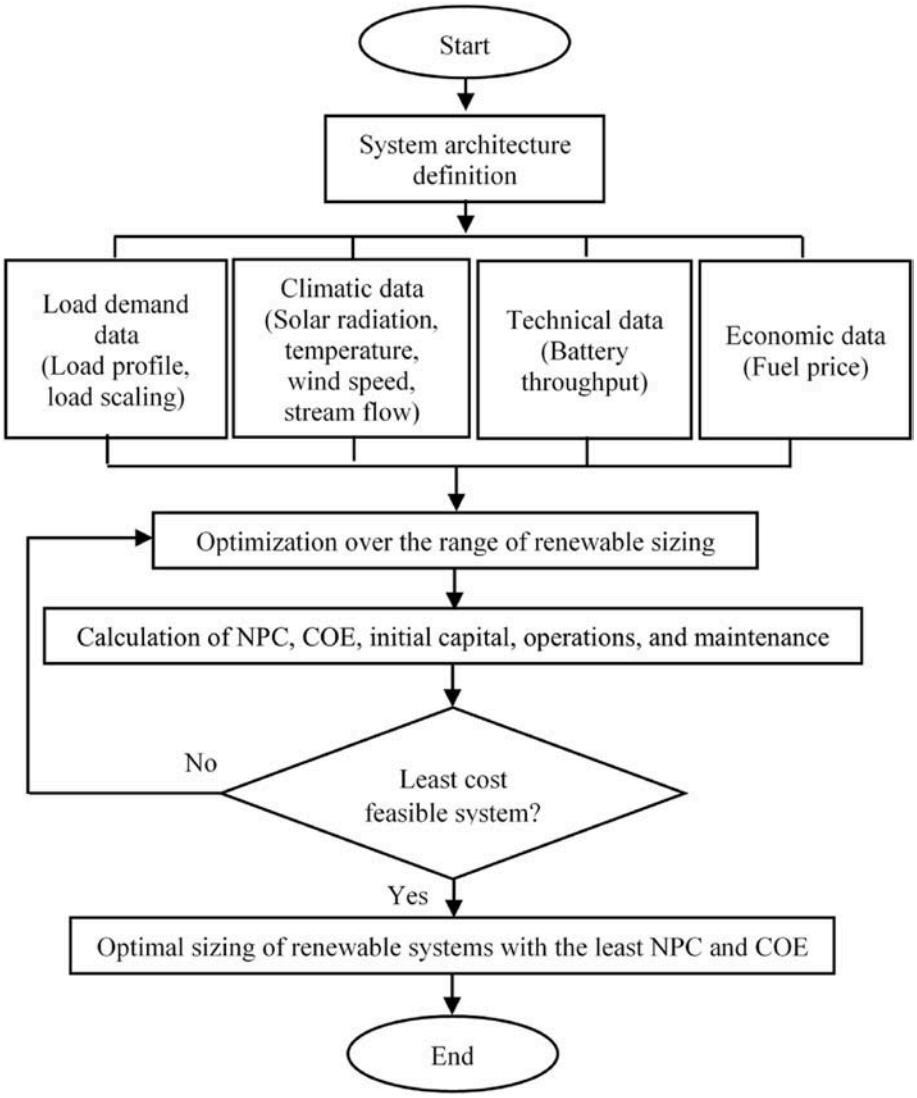

Fig. 7. Optimal component sizing of renewables for the multi-terminal MVDC system.

$$SI = \left(\frac{\Delta y}{\Delta x}\right) \tag{33}$$

Fig. 7 depicts the overall methodological framework adopted for the techno-economic assessment of the proposed multi-terminal MVDC system. The process begins with defining the system architecture, where the configuration of AC/DC terminals, converter ratings, interconnection layout, and control hierarchy are established. This setup ensures that all system components and operational limits of the network are properly represented before any economic optimization is performed. Subsequently, four principal categories of input data are prepared. The load demand data captures the temporal variation of both AC and DC loads within the MVDC network, incorporating hourly load profiles and relevant load-scaling factors. These inputs represent realistic operating conditions for residential, commercial, and industrial consumers. The climatic data include solar irradiance, temperature, wind speed, and stream flow, which define the availability and variability of renewable energy resources throughout the year. The technical data specify the performance characteristics of individual system components, including converter and inverter efficiencies, transformer losses, allowable battery throughput, depth-of-discharge limits, and degradation factors that affect component lifetime and replacement intervals. The economic data encompass the capital, replacement, and maintenance costs of each component, as well as fuel prices and escalation rates. Once all input parameters are defined, the optimization process is executed to determine the most economically feasible configuration of renewable and storage components. The optimization is performed over a predefined range of component sizes. For each configuration, the model evaluates key economic indicators, including NPC, Levelized COE, Initial Capital Cost, Operating Cost, Maintenance Cost (O&M), Replacement Cost, and Return on Investment (ROI). The optimization applies a load-following dispatch strategy, dynamically adjusting generation and storage operation to meet instantaneous load demand while minimizing energy curtailment and unmet load. The iterative process continues until convergence is achieved on a configuration that satisfies all technical constraints and results in the minimum NPC and COE with an acceptable ROI.

4. Real-time process monitoring

To enhance the operational functionality and visibility of the proposed MVDC system, a cloud-based real-time monitoring and feedback platform was developed using an IoT architecture integrated with MATLAB-Simulink. The main objective of this platform is not only to collect and visualize system parameters but also to exchange live operational data between the physical hardware layer and the simulated MVDC model, enabling real-time validation and adaptive control

assessment. This integration ensures that the Simulink-based control strategy continuously reflects the real-time operating conditions of the physical system, allowing coordinated adjustment of converter reference voltages, voltage regulation, and power-sharing functions. By enabling closed-loop interaction between measurement, cloud communication, and control response, the IoT framework transforms the MVDC setup from a passive monitoring system into an active decision-support platform capable of adaptive operation. Fig. 8 illustrates the overall architecture and data flow of the integrated monitoring system. In the experimental configuration, the Arduino Mega 2560 microcontroller [57] is interfaced with a DC voltage sensor to continuously measure the instantaneous terminal voltage of the battery bank connected to the MVDC bus. The measured analog signals are converted into digital data and transmitted to the NodeMCU V3 microcontroller through UART serial communication. The NodeMCU, featuring the ESP8266 Wi-Fi module, connects to the Internet and transfers data packets to the ThingSpeak cloud server using a Hypertext Transfer Protocol-based Application Programming Interface (HTTP-API) [58]. The Arduino Integrated Development Environment (IDE) is used to program both microcontrollers, enabling automated data acquisition, scaling, and packet transmission. To safely measure higher voltages, Arduino's analog input range of 0–5 V requires the use of a voltage divider network consisting of R1 = 30 kΩ and R2 = 7.5 kΩ [59]. The measured DC voltage can be expressed in (34). This configuration allows accurate sensing of voltages up to 25 V with minimal signal distortion. The NodeMCU V3, powered at 3.3 V and protected by an internal regulator up to 20 V, ensures stable data transmission to the cloud with an average update interval of 20 s [60]. The live solar irradiance data is collected every 10 min, as stated in Ref. [61], while the DC voltage of the battery is monitored on ThingSpeak with a 20-s update interval. The ThingSpeak cloud platform serves as the central data repository and visualization interface, allowing bidirectional communication between the physical sensors and the MATLAB-Simulink-based MVDC model. Two functional blocks (ThingSpeak Write and ThingSpeak Read) are employed within Simscape to establish a live data exchange loop:

1) The Write block exports simulated DC voltages and currents from Simulink to the ThingSpeak dashboard for real-time visualization.
2) The Read block retrieves actual sensor data from ThingSpeak and dynamically injects it into the Simulink model, thereby creating a hardware-in-the-loop (HIL) feedback environment.

$$V_{DC}^{measured} = \frac{V_{DC}^{Arduino}}{\frac{R2}{R1+R2}} \tag{34}$$

This configuration enables the MVDC controller to modify converter reference voltages, adjust droop coefficients, and alter state-of-charge

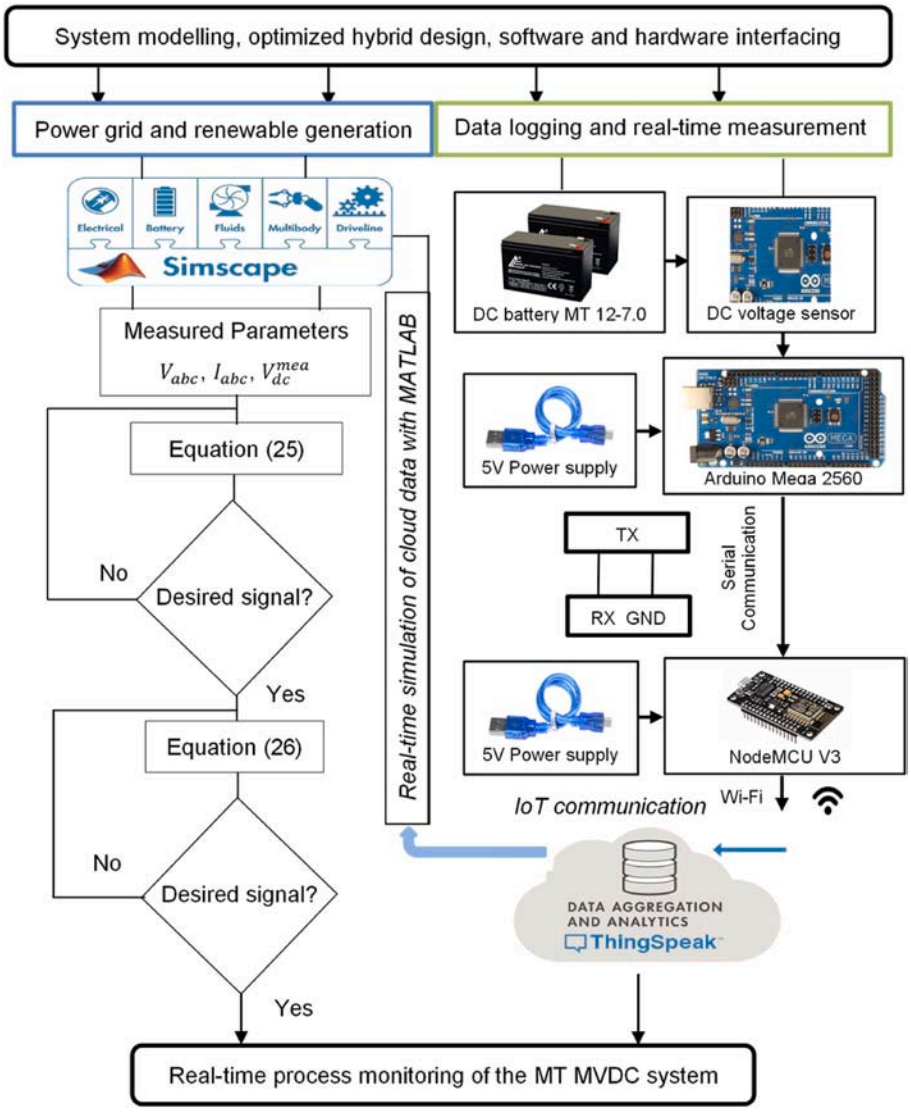

Fig. 8. Integrated condition monitoring platform for MT MVDC system.

control signals based on the most recent measured data. In other words, the IoT data directly influences the operational response of the MVDC system during simulation, enabling the evaluation of how the system behaves under real environmental and loading conditions. Through this integrated design, the IoT-Simulink coupling provides a synchronized digital twin representation of the MVDC network, supporting real-time condition awareness and facilitating future extensions toward predictive maintenance and autonomous operation. The developed IoT framework, therefore, establishes a fully integrated monitoring and feedback architecture that links physical measurements, cloud communication, and real-time simulation. It provides the technical foundation for remote observability, adaptive control testing, and further performance evaluation discussed in the subsequent results section.

5. Results and discussion

This section presents the results of test scenarios to verify the response of the proposed multi-terminal medium voltage design under steady-state and fault conditions. MATLAB Simulink (R2022b) and HOMER software were used in tandem to design and evaluate the MTDC system. Simulink is used for the system design and performance evaluation, while HOMER is employed for techno-economic analysis to determine the most efficient configuration. The ThingSpeak cloud platform for IoT and MATLAB Simscape are utilized as tools to incorporate data parameters and monitor system conditions. The MATLAB and HOMER software are installed on a desktop computer with Microsoft Windows 10 Pro 64-bit Operating System (OS), Intel(R) Core (TM) i7-9700 CPU @ 3.00 GHz, 3000 MHz, 8 Core(s) processor, and 16 GB RAM. The experimental setup in Fig. 9 demonstrates how sensors bridge the gap between the digital and physical worlds by gathering data from hardware components. The information received by the ThingSpeak cloud platform over the internet includes data on energy storage and renewable energy. The MTDC system is connected to the internet constantly to receive and send data that can be processed on the IoT cloud server. The following subsections present the results and detailed discussion for the operational and economic performances of the proposed design.

5.1. Performance of MVDC design during steady state condition

The system operates stably under steady-state conditions with an AC terminal voltage of 11 kV and a DC reference voltage of 15 kV, as illustrated in Fig. 10(a and b). In Fig. 10 (a), the RMS voltages at the AC terminals, V_{rms}^{grid}, V_{rms}^{wind}, and V_{rms}^{hydro} are 11.11 kV, 11.15 kV, and 11.29 kV, respectively, after passing through the transformers shown in Fig. 2. Here, the deviation from rated AC voltage is less than 3 %. Fig. 10 (b) presents the corresponding DC terminal voltages V_{DC}^{grid}, V_{DC}^{wind}, V_{DC}^{PV}, V_{DC}^{hydro}, and V_{DC}^{batt} are 14.99 kV, 15.04 kV, 14.97 kV, 15.33 kV, and 15.28 kV, respectively. These voltages are obtained from the MTDC terminals after passing through voltage source converters (for the grid, wind, and hydro units), a DC-DC converter (for the battery terminal), and directly from the solar source, as illustrated in Fig. 2. The deviations from the 15 kV reference DC voltage are also within 3 %, confirming that the system maintains stable and balanced operation under steady-state.

5.2. Performance of MVDC design during fault condition at AC and DC sides

Fig. 11 shows the results of a three-phase fault applied to the AC side of the power grid. This fault initiated at time 1.5 s and lasted for 0.1 s. Afterward, the fault condition was repeated for the wind terminal as illustrated in Fig. 12. In the scenario described, the condition of the MTDC system was monitored in real-time using a Thingspeak channel, with the data visualized in Fig. 13(a and b). Referring to Figs. 11 and 12, it is seen that the AC voltage and current fluctuations when the fault occurs at the power grid and wind turbine terminals are similar. Once the fault happened, the voltages of the power grid and wind turbine terminals dropped to zero. On the other hand, the currents have increased significantly to a high value. After the fault had been cleared, the system returned to steady state after 1.6 s. The values of voltage at the AC side vary from 11.10 kV to 11.34 kV, while the DC voltage values are 14.80 kV and 15.31 kV after the fault has been cleared. Overall, the deviations from the nominal voltage levels remained below 3.1 %, indicating that the system successfully restored stable operation following the disturbance. It is worth noting that the DC side voltage and current changes are minimal during an AC fault, making AC faults less impactful on the DC side. The DC voltages and currents have also been recovered to normal after the fault was cleared, as shown in Figs. 11 and 12. The negative DC currents in Figs. 11 and 12 show that the currents are flowing in the fault direction. The results of this scenario indicate that the proposed design performs well under AC fault conditions.

Sequentially, a pole-to-pole DC short-circuit fault was applied at the PV solar terminal bus. Figs. 14 and 15 depict the corresponding deviations in AC and DC voltages and currents at both the non-PV DC bus and the PV terminal bus, respectively. The system's condition is monitored through a Thingspeak channel, as illustrated in Fig. 16(a and b). These figures show that after the fault is cleared, the system gradually returns to a stable operating condition, achieving a steady state at 2.0 s. Here, the DC fault impacts the AC side of the system, and the AC currents are also being drawn to the DC fault location due to the ring topology. However, the AC voltages and currents are normalized after the fault is cleared, as shown in Figs. 14 and 15. The voltages on the AC side vary between 11.09 kV and 11.22 kV, while the DC voltages range between 14.78 kV and 15.22 kV after the fault is cleared. The deviations from the nominal voltage levels were within 2.2 %, demonstrating that the

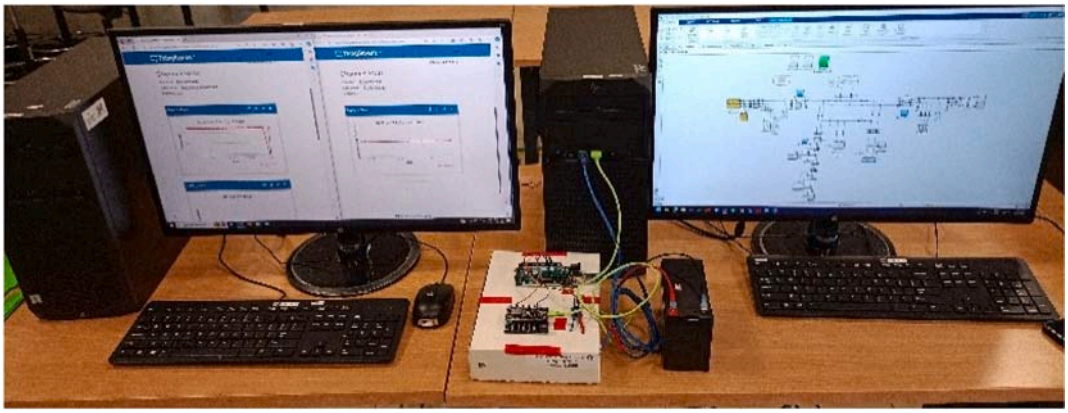

Fig. 9. Experimental setup consisting of cloud-based IoT and I/O interface connected with Simulink.

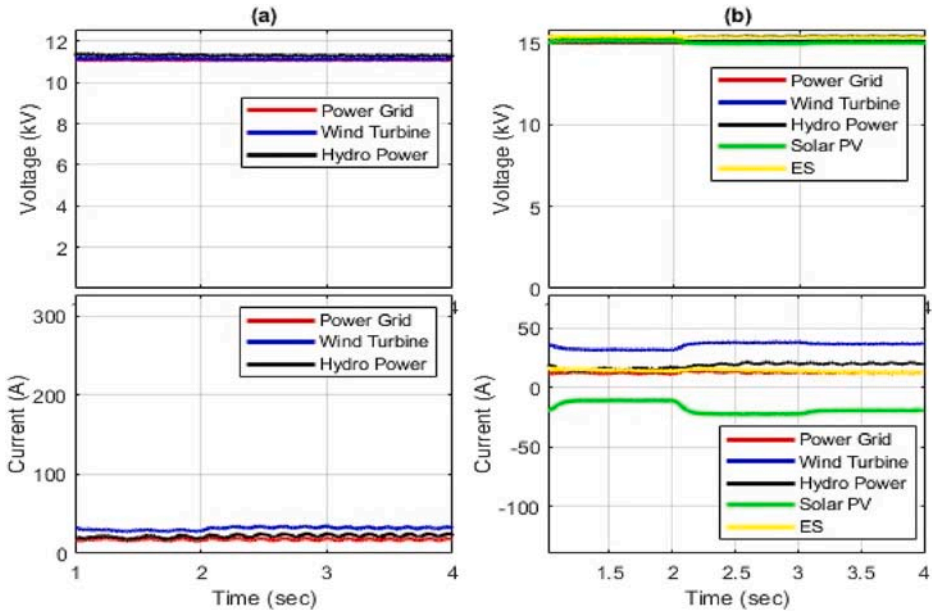

Fig. 10. RMS voltage and current: (a) AC side; (b) DC side.

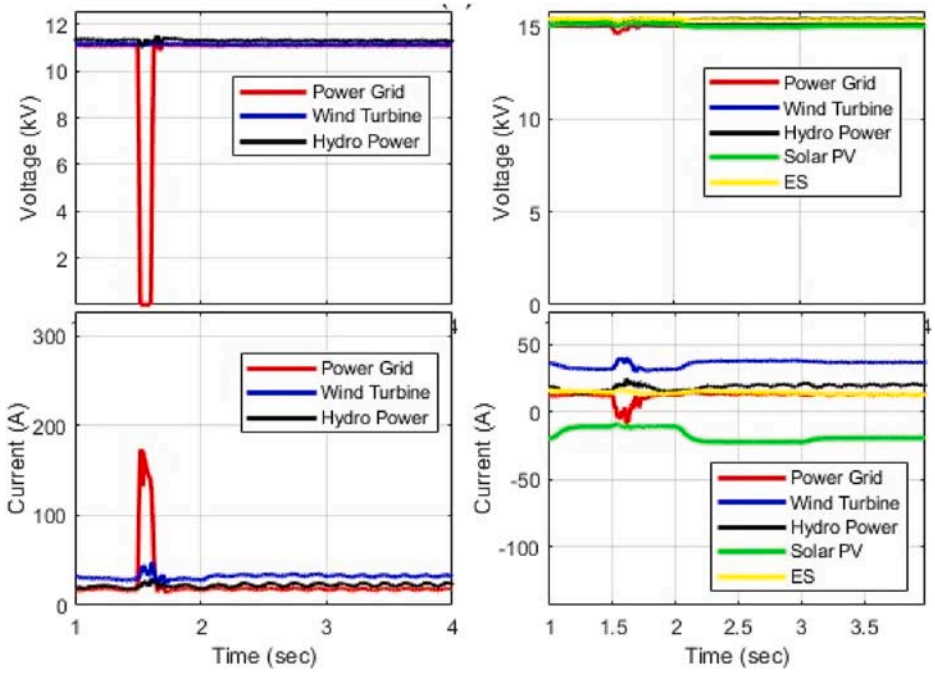

Fig. 11. MTDC system during an AC fault at the power grid terminal.

proposed system maintains stability and quickly restores normal operation. These results confirm the robustness and reliability of the proposed MVDC configuration under severe DC fault conditions.

Overall, the proposed MTDC system demonstrates strong robustness and resilience under both AC and DC fault conditions. Specifically, the system successfully restores normal operation with a maximum voltage deviation of approximately 3.1 % following AC fault recovery and as low as 2.2 % after DC fault recovery. These results indicate that the proposed configuration effectively maintains voltage stability, ensures rapid dynamic response, and achieves reliable post-fault voltage regulation across both AC and DC terminals.

5.3. Techno-economic assessment of MVDC models

The outcomes of the techno-economic analysis are discussed in this subsection with emphasis on the cost of energy, total production, excess electricity, unmet electric load, and pollutant emissions. Different models have been examined in terms of powering loads by optimizing various configurations to ensure that the system meets the peak loads. Fig. 17 shows the daily load and scaled annual average (SAA) profiles selected for specific days of each month, incorporating random variabilities with a load factor of 30 % utilized in Simulink. The SAA in HOMER is a setting that allows you to adjust the overall magnitude of a load or resource profile, such as wind speed or electrical demand, while maintaining its shape and temporal characteristics unchanged. Table 3

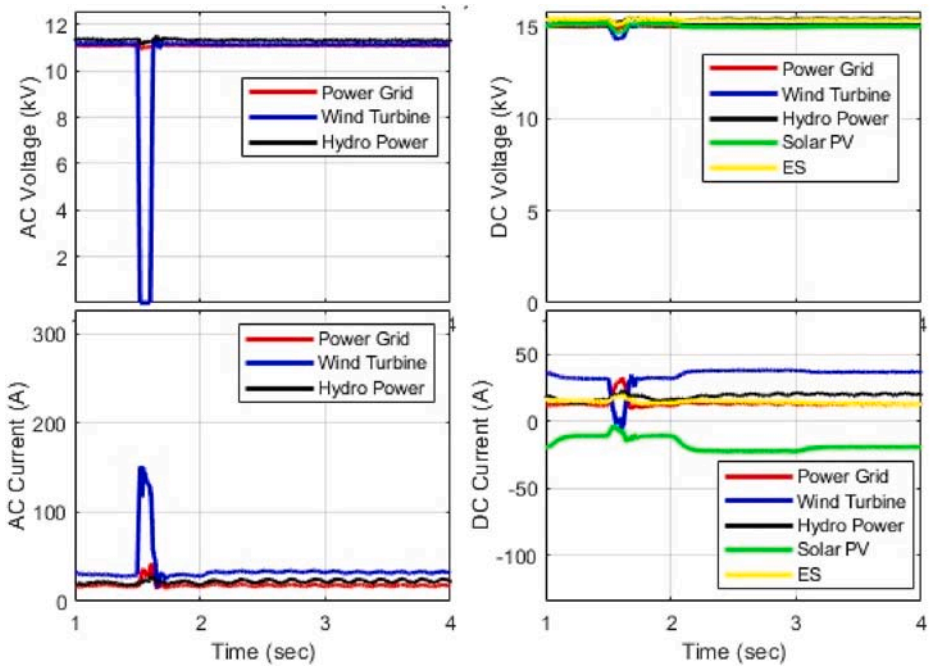

Fig. 12. MTDC system during an AC fault at the wind turbine terminal.

Fig. 13. MTDC condition monitoring during AC fault: (a) voltage "DC"; (b) current "DC".

illustrates the optimal capacity of components, considering that AC or DC loads are powered by hybrid renewable MTDC systems located in different places. The battery serves as energy storage to capture excess electricity generated by the solar PV array to meet the load demand.

The economic feasibility analysis of the optimized MTDC system is demonstrated in Table 4. Here, the NPC and levelized COE for model 4 are the highest values among the other models. Following model 4, the LCOE is progressively lower for models 3, 2, and 1. It is also observed that the capital cost for the first model is the highest ($47,634,321.83), since the total installed capacity of photovoltaic panels and conversion systems is the highest among other renewable sources. In the four analyzed models, the annual operating cost is high in both models (3 and 4), where the installed renewable generation capacity is the lowest. There is a slight difference in the return on investment (ROI) between the four models.

The energy production of each optimized configuration has also been analyzed, as illustrated in Table 5. It can be concluded that the renewable energy contribution in models 1 and 2 is the highest compared to models 3 and 4. As seen in Table 5, the highest unmet electric load is (0.0165 %) in model 4, where the main source of energy production from solar PV is (5,630,781 kWh/year). The absence of energy storage can lead to energy shortages. Hence, installing energy storage as in models 1 and 2 would increase energy production. The power grid in all models is indeed presumed as a backup source to ensure that AC and DC loads in the MTDC system are continuously supplied with power. Referring to Table 5, the unmet load percentage (0–0.0165 %) quantifies the portion of the total demand that could not be supplied, indicating the adequacy of the MTDC system in meeting continuous load requirements across all configurations. The excess energy percentage (up to 8 %) reflects the system's capability to handle surplus renewable generation, thus representing operational flexibility and resilience in energy management and storage utilization. Together, these parameters act as reliability indices that evaluate both the technical performance and resilience of the proposed MVDC network, confirming its ability to maintain stable operation and ensure power adequacy under varying grid and fault conditions.

As the use of renewable energy resources mainly for electric transport can certainly help reduce pollutant emissions, environmental feasibility analysis has been carried out to evaluate pollution levels, considering four models as depicted in Table 6. Here, the power generated from renewable generation in the MTDC model not only meets the AC and DC loads but also decreases environmental pollution. For instance, the annual emissions of carbon dioxide in models 1 and 2 are 15,198,763 kg/year and 15,438,953 kg/year, respectively. Note that the AC and DC loads in these models are also supplied from the electricity grid. Furthermore, a small amount of sulfur dioxide and nitrogen

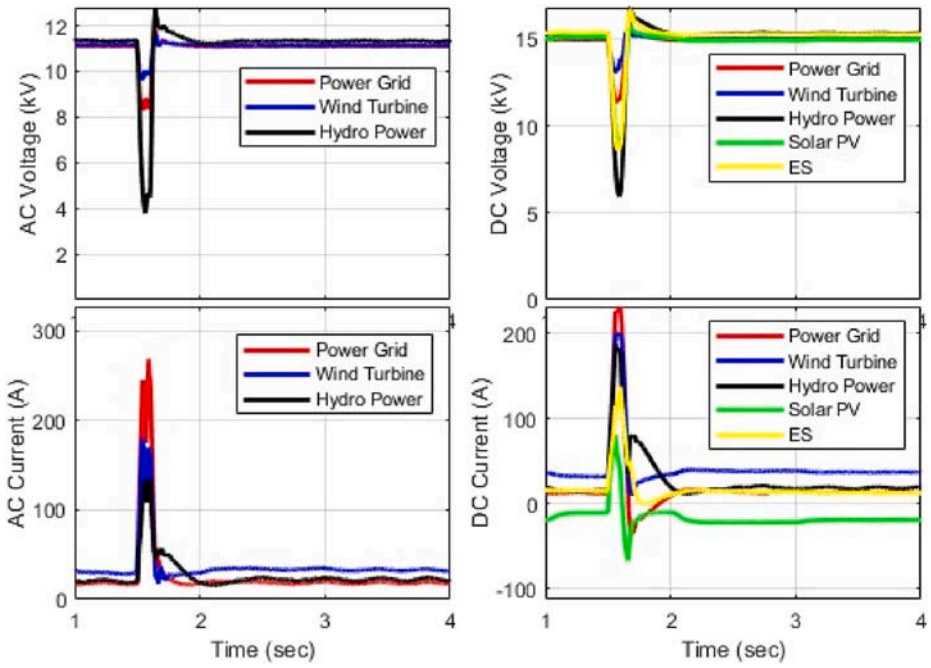

Fig. 14. MTDC system during fault at DC bus.

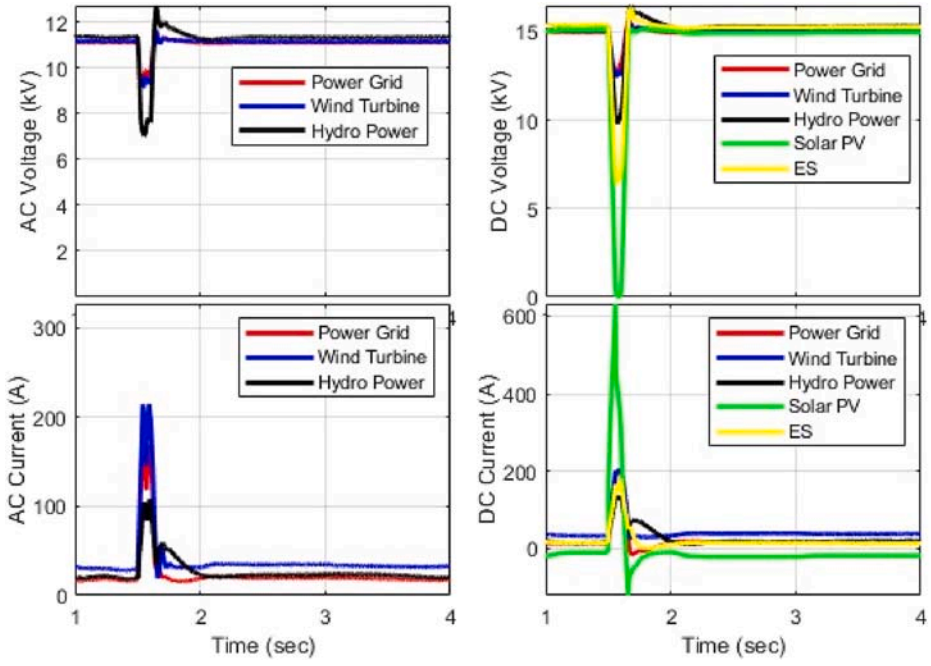

Fig. 15. MTDC system during DC fault at PV solar terminal.

oxides is indeed emitted from the power grid yearly in the first model (37,218 kg and 89,998 kg), and in the second model (37,806 kg and 91,421 kg). The highest annual amount of carbon monoxide produced by conventional sources in the power grid is in the third model (137,083 kg/year) and the fourth model (135,346 kg/year). In general, the levels of emissions from the MTDC system in the first and second models are lower compared with the third and fourth models. Table 7 demonstrates the energy losses in the MTDC models with different configurations. It can be observed that energy losses are lowest for the system converters in the third and fourth models.

5.4. Sensitivity analysis of MVDC design

To address the unavoidable uncertainty in renewable generation, sensitivity analyses are performed on the optimal configuration to investigate the possible change in the cost of energy when varying the parameters of solar radiation, wind speed, water flow rate, fuel price, and temperature. The effects of the variations on the COE are shown in Fig. 18. The presented sensitivity analysis investigates the impact of varying the above-mentioned parameters in the range of (−30 %–30 %) on the optimized MV MTDC model. The optimized model should fulfill the total maximum load demand of the AC side (3.27 MW) and the DC side (2 MW). The assessment specifically reflects changes in solar

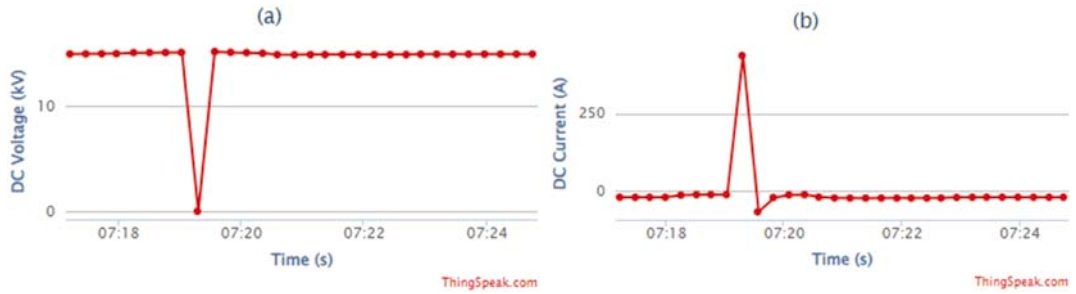

Fig. 16. MTDC condition monitoring during DC fault: (a) voltage "DC"; (b) current (DC).

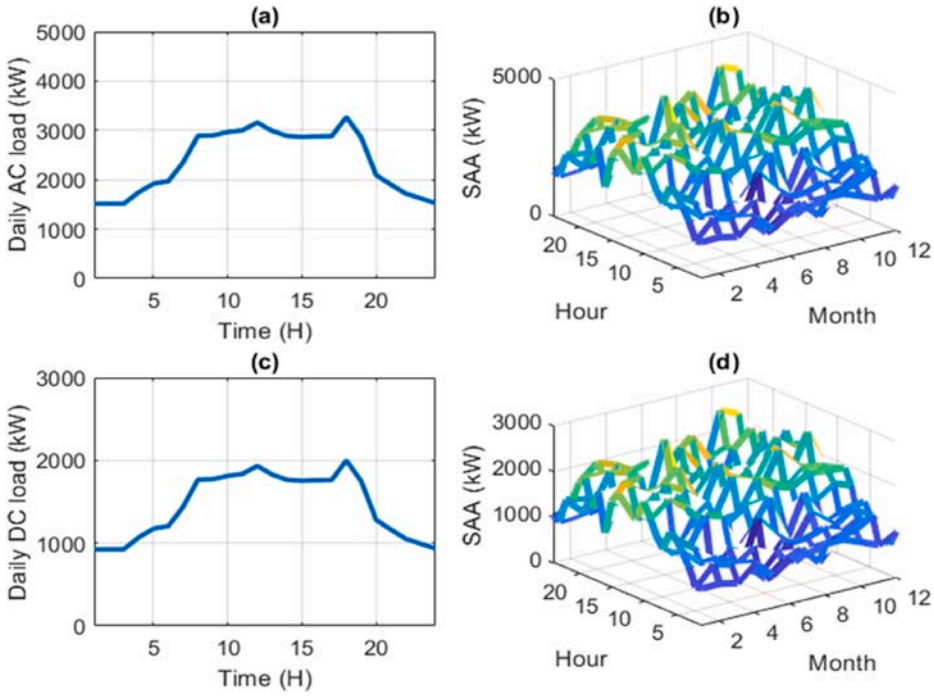

Fig. 17. Load profiles: (a) AC daily load; (b) scaled annual average of AC load; (c) DC daily load; (d) scaled annual average of DC load.

Table 3
Optimized capacity of components in the MTDC models.

Components	Models			
	1	2	3	4
Solar panel (kW)	13,514	12,764	4050	4595
Wind generator (kW)	0	10.0	0	60.0
Hydro generator (kW)	11	11	11	11
AC Load Average (kW)	2372.5	2372.5	2372.5	2372.5
DC Load Average (kW)	1451.1	1451.1	1451.1	1451.1
Power grid (kW)	∞	∞	∞	∞
Energy Storage (kWh)	24,821	25,816	0	0

radiation, water flow rate, fuel price, and temperature within the context of model "1". As wind power is absent in model "1", wind speed variations are extrapolated from the scenario of the second model. Fig. 18 shows changes in solar radiation led to a significant reduction in the COE, from $0.4406 to $0.3923. In contrast, changes in wind speed have no discernible effect on COE, maintaining a value of 0.4114 within a range of (−30 %–30 %). Similarly, variations in water flow rate result in marginal COE decrements, ranging from $0.41145 to $0.41143. The fuel price parameter has a more pronounced impact, causing a linear increase in the Levelized COE from $0.3597 to $0.4629. Here, the temperature parameter variations are visibly affecting the COE, gradually increasing from $0.4082 to $0.4148. The analysis also reveals an inherent pattern where a higher integration of typical energy sources

Table 4
Cost summary of the MTDC models.

Relevant costs	Model 1	Model 2	Model 3	Model 4
Net Present Cost ($)	178,156,000	178,515,700	191,786,200	192,220,200
Levelized COE ($/kWh)	0.4114	0.4123	0.4430	0.4440
Operating cost ($/year)	10,096,420	10,238,190	13,607,700	22,046,220
Maintenance cost (O&M) ($/year)	2,063,653.02	2,092,218.62	2,592,057.21	2,600,511.50
Replacement cost ($/year)	2,312,884.23	2,337,924.21	2,748,577.29	2,755,498.68
Initial Capital ($)	47,634,321.83	46,161,396.77	15,872,459.58	17,521,498.37
Return on Investment ROI (%)	6.8	6.9	6.4	5.7

Table 5
Summary of electrical energy production in the MTDC models.

Energy production (kWh/year)	Model 1	Model 2	Model 3	Model 4
Solar PV system	16,559,352	15,641,253	4,962,427	5,630,781
	43.8 %	42.0 %	14.2 %	16.0 %
Wind generator	0	1194	0	7161
	0 %	0.00321 %	0 %	0.0203 %
Hydro generator	122,716	122,716	122,716	122,716
	0.325 %	0.330 %	0.351 %	0.348 %
Grid purchases	21,128,928	21,464,715	29,925,265	29,479,091
	55.9 %	57.7 %	85.5 %	83.7 %
Total production	37,810,996	37,229,878	35,010,408	35,239,749
	100 %	100 %	100 %	100 %
Renewable energy contribution	44.125 %	42.33321 %	14.551 %	16.3683 %
Excess electricity	3,032,362	2,457,868	1,069,192	1,309,018
	8.02 %	6.60 %	3.05 %	3.71 %
Unmet electric load	0	0	4512	5519
	0 %	0 %	0.0135 %	0.0165 %

Table 6
Emissions with different configurations of MTDC models.

Pollutant types	Emissions (kg/year)			
	Model 1	Model 2	Model 3	Model 4
Carbon dioxide (CO_2)	15,198,763	15,438,953	21,747,327	21,471,728
Carbon monoxide (CO)	95,805	97,319	137,083	135,346
Sulfur dioxide (SO_2)	37,218	37,806	53,254	52,579
Nitrogen oxides (NO_x)	89,998	91,421	128,775	127,143

Table 7
Energy losses in the MTDC models with different configurations.

Losses (kWh/year)		Model 1	Model 2	Model 3	Model 4
System Converter	Inverter	402,611	390,150	10,938	17,773
	Rectifier	402,126	406,900	439,257	422,944
Energy Storage		478,366	479,430	N/A	N/A

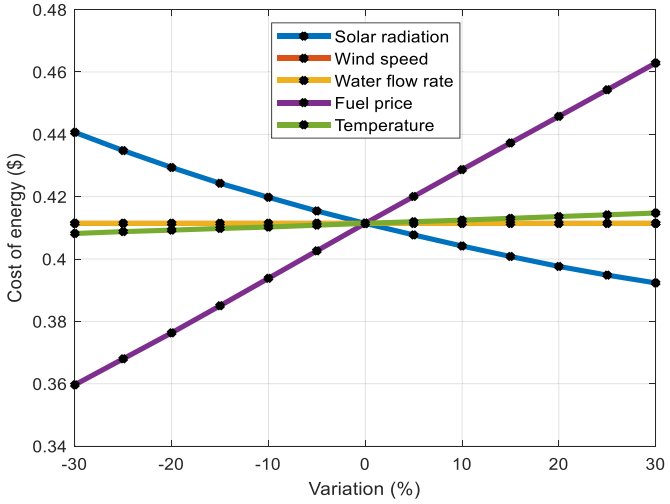

Fig. 18. Effects of solar radiation, wind speed, water flow rate, fuel price and temperature.

correlates with more substantial COE deviations. For example, introducing 43.8 % solar PV power in model "1" leads to significant COE changes. Similarly, a notable escalation in COE is observed with the utilization of a high percentage of grid power (55.9 %). In contrast, the limited utilization of hydropower (0.325 %) in the first model and the minimal incorporation of wind power (0.00321 %) in the second model have only negligible implications for COE deviations.

It is worth mentioning that the proposed MV MTDC system for the first and second models can produce more DC power from solar PV systems, emphasizing the necessity to evaluate the impact of energy storage on profitability. Hence, sensitivity analysis has been conducted by altering the energy throughput (kWh) of the storage system. The energy throughput parameter is chosen because it affects the battery cycle life, durability, economic viability, return on Investment, frequency of replacement, and other values. A sensitivity scenario was performed for the first model, which is considered the best option, and the results are depicted in Fig. 19. Based on the optimization results generated from the HOMER algorithm, the dispatch strategy for energy throughputs of 500 kWh and 600 kWh is load following (LF), while energy throughputs exceeding 600 kWh utilize cycle charging (CC) strategies. The preference for LF in low-throughput scenarios is due to its ability to reduce cycling stress, resulting in less frequent charging and discharging, thus extending the lifetime of energy storage. Referring to Fig. 19, the sensitivity analysis illustrates the variations in energy throughputs (from 500 kWh to 1000 kWh) and their impact on capital cost ($), energy storage size (kWh), simple payback (years), and ROI (%). In this regard, the 500 kWh energy throughput emerges as a well-balanced option, featuring a moderate capital investment of $7,401,300.00 with a battery size of 24,671 kWh, and a reasonable payback period of 6.76 years, coupled with a fair return on investment of 8.2 %. In contrast, the 600 kWh energy throughput necessitates the highest capital investment at $8,305,800.00, resulting in a larger battery size (27,686 kWh) and a relatively extended payback period of 8.15 years. The 700 kWh system displays a competitive return on investment at 8.8 %, despite a lower capital cost of $6,876,900.00 and a shorter payback period of 6.67 years. Furthermore, the 1000 kWh system, with a capital investment of $7,306,500.00, yields a battery size of 24,355 kWh and a return on investment of 9 %. Notably, this analysis highlights the exceptional performance of the 900 kWh energy throughput. It combines a respectable capital investment of $7,247,100.00, delivering a battery size of 24,157 kWh with promising benefits. These include the lowest simple payback period (6.67 years) and the highest percentage of ROI (9 %) among the other options.

6. Conclusion

An economical design of a multi-terminal medium-voltage DC (MTDC) distribution system with an effective generalized droop control strategy has been proposed for distribution and transportation networks. The suggested topology, combined with the control algorithm, was verified under various operating conditions using a real-time cloud monitoring environment. The main contributions and findings are summarized as follows:

- Operational analyses demonstrate that the proposed approach effectively maintains DC voltage deviations within 3 % under steady-state conditions, 3.1 % following AC three-phase faults, and as low as 2.2 % after DC pole-to-pole short-circuit events, demonstrating robust operation under various disturbances.
- The techno-economic analysis confirms that the costs of reducing emissions and enhancing system reliability are directly proportional to the total net present cost, while the system achieves a low levelized cost of energy (LCOE) of 0.4114 $/kWh and a renewable energy penetration of up to 44 %.
- Reliability metrics show that the unmet load percentage is extremely low (0–0.0165 %), and excess energy remains manageable (up to 8 %), indicating the system can meet demand efficiently while accommodating renewable generation.
- Environmental assessments reveal that the MTDC system reduces CO_2, SO_2, NO_x, and CO emissions compared with conventional grid

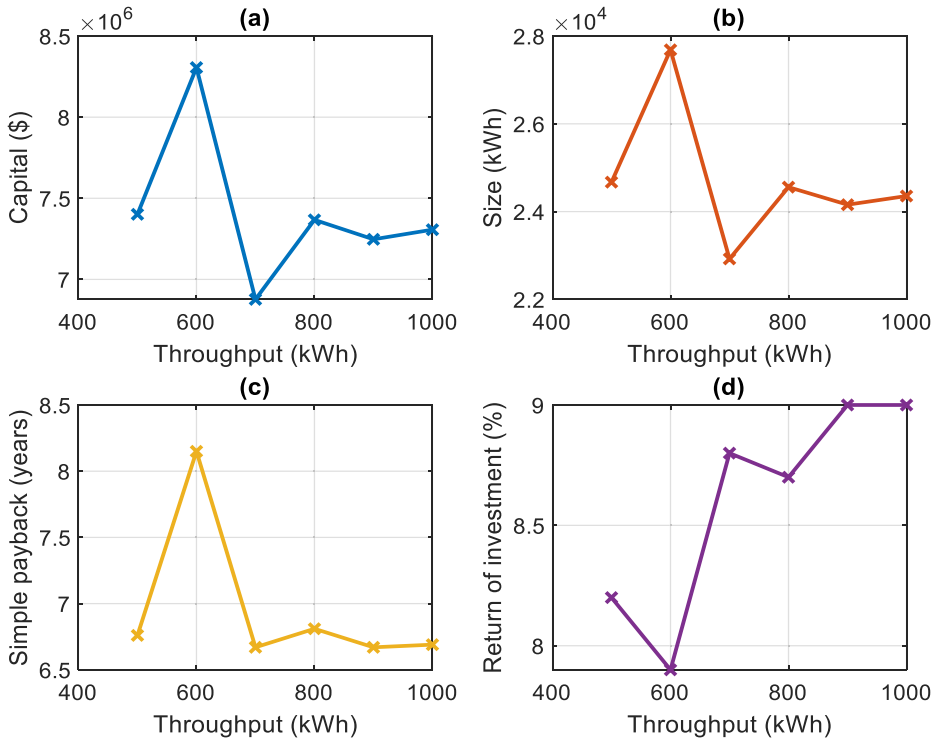

Fig. 19. Energy throughput analysis: (a) Capital; (b) Battery size; (c) Simple payback; (d) ROI.

reliance, highlighting its contribution to sustainable energy integration.
- The existing cloud-based monitoring platform provides valuable insights into system performance, enabling early detection of potential issues, enhancing efficiency, reliability, and reducing maintenance costs and downtime.

As MTDC systems become more widespread, it is essential to establish standards for interoperability and communication between different systems, in particular when optimizing the location of renewable energy storage systems [62]. Future scope will address these limitations through the following directions:

- Extend the system study to large-scale and geographically dispersed MTDC networks to evaluate scalability, communication delay, and stability under diverse grid conditions.
- Conduct field-based experimental validation of the techno-economic model to refine cost and emission parameters for practical deployment.
- Enhance the IoT-based monitoring framework with improved cybersecurity measures, data encryption, and offline fault-tolerant data storage for reliable operation in remote areas.
- Develop standardized communication protocols and interface tools to improve interoperability between different MTDC systems and ensure seamless integration with the existing power grid.

In summary, the proposed framework lays a foundation for future research on resilient, scalable, and digitally integrated MVDC networks that can effectively support the expansion of renewable energy in modern power systems.

CRediT authorship contribution statement

M.M. Ahmed: Supervision, Resources, Project administration, Funding acquisition. **F.C. Jong:** Visualization, Validation, Software, Data curation. **Lau Wei Kin:** Writing – original draft, Software, Methodology, Formal analysis. **Ahmed M.A. Haidar:** Writing – review & editing, Validation, Supervision, Software, Investigation, Formal analysis, Conceptualization.

Declaration of competing interest

The authors declare that they have no known competing financial interests or personal relationships that could have appeared to influence the work reported in this paper.

Acknowledgment

The authors acknowledge the support of the Sarawak State Government under the Digital Sarawak CoE grant (UHSB/B-AM2018/090) and Universiti Malaysia Sarawak for providing the necessary facilities for this study. The authors also wish to thank the editor and anonymous reviewers for their time and effort in reviewing the manuscript.

References

[1] Ahmad Shah Ayobe, Surbhi Gupta, Comparative investigation on HVDC and HVAC for bulk power delivery, Mater. Today Proc. 48 (Part 5) (2022) 958–964.
[2] H. Xiao, K. Sun, J. Pan, L. Xiao, C. Gan, Y. Liu, Coordinated frequency regulation among asynchronous AC grids with an MTDC system, Int. J. Electr. Power Energy Syst. 126 (2021) 106604.
[3] H. Xiao, K. Sun, J. Pan, Y. Li, Y. Liu, Review of hybrid HVDC systems combining line communicated converter and voltage source converter, Int. J. Electr. Power Energy Syst. 129 (2021) 106713.
[4] D. Jovcic, High Voltage Direct Current Transmission: Converters, Systems and DC Grids, John Wiley & Sons, 2019.
[5] P.K. Kushwaha, C. Bhattacharjee, An extensive review of the configurations, modeling, storage technologies, design parameters, sizing methodologies, energy management, system control, and sensitivity analysis aspects of hybrid renewable energy systems, Elec. Power Compon. Syst. 51 (20) (2023) 2603–2642.
[6] P.K. Kushwaha, C. Bhattacharjee, Socio-techno-economic-environmental sizing of hybrid renewable energy system using metaheuristic optimization approaches, Environ. Prog. Sustain. Energy 43 (3) (2024) e14386.
[7] S. Jarjees Ul Hassan, Arif Mehdi, Zeeshan Haider, Jin-Sol Song, Arefaynie D. Abraham, Gwang-Su Shin, Chul-Hwan Kim, Towards medium voltage hybrid AC/DC distribution systems: architectural topologies, planning and operation, Electrical Power and Energy Systems 159 (2024) 110003.

[8] D. Altun, Examination of Different Communication Topologies for Distributed Control of multi-terminal HVDC Grids, 2019.
[9] M.K. Bucher, R. Wiget, G. Andersson, C.M. Franck, Multiterminal HVDC networks—What is the preferred topology, IEEE Trans. Power Deliv. 29 (1) (2013) 406–413.
[10] Z. Li, R. Zhan, Y. Li, Y. He, J. Hou, X. Zhao, X.P. Zhang, Recent developments in HVDC transmission systems to support renewable energy integration, Global Energy Interconnection 1 (5) (2018) 595–607.
[11] C. Guo, C. Li, C. Zhao, X. Ni, K. Zha, W. Xu, An evolutional line-commutated converter integrated with thyristor-based full-bridge module to mitigate the commutation failure, IEEE Trans. Power Electron. 32 (2) (2016) 967–976.
[12] Y. Xue, X.P. Zhang, C. Yang, Commutation failure elimination of LCC HVDC systems using thyristor-based controllable capacitors, IEEE Trans. Power Deliv. 33 (3) (2017) 1448–1458.
[13] S.R. Mohammed, J. Teh, M.K.M. Jamil, Reliability and power density increase in a novel four-pole system for line-commutated converter HVDC transmission, IEEE Access 7 (2019) 10057–10076.
[14] Y. Xue, X.P. Zhang, C. Yang, AC filterless flexible LCC HVDC with reduced voltage rating of controllable capacitors, IEEE Trans. Power Syst. 33 (5) (2018) 5507–5518.
[15] Y. Xue, X.P. Zhang, C. Yang, Series capacitor compensated AC filterless flexible LCC HVDC with enhanced power transfer under unbalanced faults, IEEE Trans. Power Syst. 34 (4) (July 2019).
[16] Y. Wang, Y. Zhou, D. Li, D. Shao, K. Cao, K. Zhou, D. Cai, The influence of VSC–HVDC reactive power control mode on AC power system stability, Energies 13 (7) (2020) 1677.
[17] G.P. Adam, I. Abdelsalam, J.E. Fletcher, L. Xu, G.M. Burt, D. Holliday, S.J. Finney, Improved two-level voltage source converter for high-voltage direct current transmission systems, IEEE Journal of Emerging and Selected Topics in Power Electronics 5 (4) (2017) 1670–1686.
[18] G. Ning, W. Chen, L. Shu, J. Zhao, W. Cao, J. Mei, C. Liu, G. Qiao, A hybrid resonant ZVZCS three-level converter for MVDC-Connected offshore wind power collection systems, IEEE Trans. Power Electron. 33 (8) (2017) 6633–6645.
[19] H. You, X. Cai, A three-level modular DC/DC converter applied in high voltage DC grid, IEEE Access 6 (2018) 25448–25462.
[20] S. Dadjo Tavakoli, E. Prieto-Araujo, E. Sánchez-Sánchez, O. Gomis-Bellmunt, Interaction assessment and stability analysis of the MMC-based VSC-HVDC link, Energies 13 (8) (2020) 2075.
[21] O.E. Oni, I.E. Davidson, K.N. Mbangula, A review of LCC-HVDC and VSC-HVDC technologies and applications, in: 2016 IEEE 16th International Conference on Environment and Electrical Engineering (EEEIC), 2016, June, pp. 1–7.
[22] D. Zhang, D. Dong, R. Datta, A. Rockhill, Q. Lei, L. Garces, Modular embedded multilevel converter for MV/HVDC applications, IEEE Trans. Ind. Appl. 54 (6) (2018) 6320–6331.
[23] A. Lachichi, A. Junyent-Ferre, T.C. Green, Comparative optimization design of a modular multilevel converter tapping cells and a 2L-VSC for hybrid LV ac/dc microgrids, IEEE Trans. Ind. Appl. 55 (3) (2019) 3228–3240.
[24] P. Simiyu, A. Xin, L. Bibaya, V. Ndiyishimiye, G. Adwek, G.T. Bitew, Modelling and control of multi-terminal MVDC distribution network, in: 2018 International Conference on Power System Technology (POWERCON), IEEE, 2018, November, pp. 1–13.
[25] Y. Ji, Z. Yuan, J. Zhao, Y. Zhao, G. Li, Y. Li, Control scheme for multi-terminal VSC-based medium-voltage DC distribution networks, J. Eng. 2019 (16) (2018) 2935–2940.
[26] P. Simiyu, A. Xin, G.T. Bitew, M. Shahzad, W. Kunyu, L.K. Tuan, Review of the DC voltage coordinated control strategies for multi-terminal VSC-MVDC distribution network, J. Eng. 2019 (16) (2018) 1462–1468.
[27] Y. Suffian, A.M.A. Haidar, W.A.W.Z. Abidin, H.M. Basri, An improved hybrid method combined with a cloud-based supervisory control to facilitate smooth coordination under low-inertia grids, Progress in Engineering Science 2 (2) (2025) 1–18. Elsevier, 2025.
[28] Zineb Cabrane, Jonghoon Kim, Kisoo Yoo, Mohammed Ouassaid, HESS-based photovoltaic/batteries/supercapacitors: energy management strategy and DC bus voltage stabilization, Sol. Energy (2021) 551–563.
[29] Alberto Rios-Villacorta, Jesús Guamán-Molina, Franklin Mayorga, Diego Taipe, Platform of intelligent control of indoor lighting integrated into LVDC distribution System: a case study in the technical university of ambato, Technology and Economics of Smart Grids and Sustainable Energy 7 (2022) 26.
[30] M.Q. Khan, M.M. Ahmed, Ahmed A.M. Haidar, An accurate algorithm of PMU-based wide area measurements for fault detection using positive-sequence voltage and unwrapped dynamic angles, Measurement 192 (2022) 110906.
[31] Shuangqi Li, H. Oliver Gao, Fengqi You, AI for science in electrochemical energy storage: a multiscale systems perspective on transportation electrification, Nexus 1 (3) (2024) 100026.
[32] X. Xiang, X. Zhang, T. Luth, M.M. Merlin, T.C. Green, A compact modular multilevel DC–DC converter for high step-ratio MV and HV use, IEEE Trans. Ind. Electron. 65 (9) (2018) 7060–7071.
[33] Dan Zhaohui, Aoye Song, Yuyu Zheng, Xinyue Zhang, Yuekuan Zhou, City information models for optimal EV charging and energy-resilient renaissance, Nexus 2 (1) (2025) 100056.
[34] A. Adhikaree, T. Kim, J. Vagdoda, A. Ochoa, P.J. Hernandez, Y. Lee, Cloud-based battery condition monitoring platform for large-scale lithium-ion battery energy storage systems using internet-of-things (IoT), in: 2017 IEEE Energy Conversion Congress and Exposition (ECCE), IEEE, 2017, October, pp. 1004–1009.
[35] A. Fakhar, A.M. Haidar, M.O. Abdullah, N. Das, Smart grid mechanism for green energy management: a comprehensive review, Int. J. Green Energy 20 (3) (2023) 284–308.
[36] M. Yigit, V.C. Gungor, S. Baktir, Cloud computing for smart grid applications, Comput. Netw. 70 (2014) 312–329.
[37] Y.W. Chen, J.M. Chang, EMaaS: cloud-based energy management service for distributed renewable energy integration, IEEE Trans. Smart Grid 6 (6) (2015) 2816–2824.
[38] G. Qiang, Y. Xi, L. Ye, Circulating current suppressing and AC faults ride-through capability analysis of zhoushan MMC-MTDC system, in: 2018 2nd IEEE Conference on Energy Internet and Energy System Integration (EI2), IEEE, 2018, October, pp. 1–6.
[39] H. Rao, Architecture of Nan'ao multi-terminal VSC-HVDC system and its multi-functional control, CSEE J. Power Energy Syst. 1 (1) (2015) 9–18.
[40] E. Kontos, R.T. Pinto, S. Rodrigues, P. Bauer, Impact of HVDC transmission system topology on multiterminal DC network faults, IEEE Trans. Power Deliv. 30 (2) (2014) 844–852.
[41] A. Raza, X. Dianguo, S. Xunwen, L. Weixing, B.W. Williams, A novel multiterminal VSC-HVdc transmission topology for offshore wind farms, IEEE Trans. Ind. Appl. 53 (2) (2016) 1316–1325.
[42] F. Mura, R.W. De Doncker, Preparation of a medium-voltage DC Grid Demonstration Project, E. ON ERC, 2012.
[43] H. Zhu, D. Xie, B. Su, M. Yang, Application of VSC and ring-topology based MTDC technology in the distribution network, in: Electrical and Control Engineering & Materials Science and Manufacturing: the Proceedings of Joint Conferences of the 6th (ICECE2015) and the 4th (ICMSM2015), 2016, pp. 151–156.
[44] G. Bathurst, G. Hwang, L. Tejwani, Mvdc-The New Technology for Distribution Networks, 2015.
[45] P.K. Kushwaha, C. Bhattacharjee, Integrated techno-economic-environmental design of off-grid microgrid model for rural power supply in India, J. Inf. Optim. Sci. 43 (1) (2022) 37–54.
[46] X. Liu, X. Mei, W. Xiang, F. Li, S. Peng, C. Zou, J. Wen, DBS-less MMC-MTDC system integrating large-scale offshore wind power, Elec. Power Syst. Res. 244 (2025) 111589.
[47] X. Zhao, C. Wang, Frequency control strategy for VSC-MTDC system based on event-triggered mechanism, Elec. Power Syst. Res. 244 (2025) 111537.
[48] Ahmed M.A. Haidar, Adila Fakhar, Kashem M. Muttaqi, An effective power dispatch strategy for clustered micro-grids while implementing optimal energy management and power sharing control using power line communication, IEEE Trans. Ind. Appl. 56 (4) (2020) 4258–4271.
[49] C.M. Young, M.H. Chen, T.A. Chang, C.C. Ko, Transformerless high step-up DC-DC converter with cockcroft-walton voltage multiplier, in: 2011 6th IEEE Conference on Industrial Electronics and Applications, IEEE, 2011, June, pp. 1599–1604.
[50] A. Kannabhiran, Transformer-Less High Step up DC-DC Converter Using Cascade Cockroft Walton Voltage Multiplier, MATLAB Central File Exchange, 2023. https://www.mathworks.com/matlabcentral/fileexchange/38027-transformer-less-high-step-up-dc-dc-converter-using-cascade-cockroft-walton-voltage-multiplier. (Accessed 25 September 2023).
[51] Pierre Giroux, Simpowersystems Model of a 1000-MW HVDC-MMC Interconnection, MATLAB Central File Exchange, 2019. Retrieved from, https://www.mathworks.com/matlabcentral/fileexchange/54506-simpowersystems-model-of-a-1000-mw-hvdc-mmc-interconnection.
[52] Y. Che, J. Zhou, W. Li, J. Zhu, C. Hong, Advanced droop control scheme in multi-terminal dc transmission systems, Journal of Electrical Engineering and Technology 13 (3) (2018) 1060–1068.
[53] Homer optimization. https://www.homerenergy.com/products/pro/docs/latest/optimization.html. Sept 202.
[54] Ahmed M.A. Haidar, Lim Wei Han, Tony Ahfock, Feasibility analysis of implementing hybrid powered electric vehicle charging stations in Sarawak, in: IEEE Sustainable Power and Energy Conference (Ispec), 2022. Australia.
[55] A. Raouf Mohamed Ahmed, Robert J. Best, Xueqin Liu, D. John Morrow, A comprehensive robust techno-economic analysis and sizing tool for the small-scale PV and BESS, IEEE Trans. Energy Convers. 37 (1) (March 2022).
[56] B. Li, J. Zhao, Y. Zhang, et al., Optimal configuration and economic operation of Wind–solar-storage complementary system for agricultural irrigation in mountainous areas, J. Electr. Eng. Technol. 18 (2023) 2649–2666, https://doi.org/10.1007/s42835-022-01373-z.
[57] Arduino mega 2560 Rev3. (n.d.). Retrieved September 30, 2022, from https://store.arduino.cc/products/arduino-mega-2560-rev3.
[58] T. Sutikno, H.S. Purnama, A. Pamungkas, A. Fadlil, I.M. Alsofyani, M.H. Jopri, Internet of things-based photovoltaics parameter monitoring system using NodeMCU ESP8266, Int. J. Electr. Comput. Eng. 11 (6) (2021).
[59] S. Kazadi, M. Thokozile, K.A. Ogudo, Design and monitoring of a voltage battery sensor of an uninterruptible power supply (UPS) by means of an arduino, in: 2020 IEEE PES/IAS Powerafrica, IEEE, 2020, August, pp. 1–5.
[60] NodeMCU v3. (n.d.). Retrieved 2022 from https://www.electronicaembajadores.com/en/Productos/Detalle/LCWFNM3/electronic-modules.
[61] Solar irradiance. (n.d.). Retrieved October 2022, from http://www.newquayweather.com/pwsWD/index.php.
[62] A.M.A. Haidar, Mohd R.M. Sharip, Tony Ahfock, An integrated decision-making approach for managing transformer tap changer operation while optimizing renewable energy storage allocation using ANP-entropy and TOPSIS, Electr. Eng. (October 2023).